Isomerization and β-scission reactions of alkanes on bifunctional metal-acid catalysts: Consequences of confinement and diffusional constraints on reactivity and selectivity

Gina Noh [a], Zhichen Shi [a], Stacey I. Zones [b], Enrique Iglesia [a,*]

[a] Department of Chemical and Biomolecular Engineering, University of California at Berkeley, Berkeley, CA 94720, United States
[b] Chevron Energy Technology Company, Richmond, CA 94801, United States

ABSTRACT

Small voids stabilize transition states through van der Waals contacts in solid acid catalysts and lead to higher reactivity as inorganic hosts and organic carbocations at transition states become similar in size and shape. Such voids also impose diffusional hurdles that can strongly influence selectivities. Bifunctional mixtures of Pt/SiO$_2$ with mesoporous or microporous aluminosilicates (Al-MCM-41, FAU, SFH, BEA, MFI) with acid sites of similar strength are used in this study to describe the consequences of confinement and diffusional constraints on isomerization and β-scission turnover rates and selectivities for n-heptane reactants. First-order rate constants (per H$^+$) for n-heptane isomerization (to primary methylhexane products) reflect free energy differences between confined carbenium ions at transition states and their gaseous alkenes precursors; they increase ($\sim$10^3-fold) as van der Waals contacts between carbocations and voids become more effective. Maximum turnover rates are achieved when their diameters, based on spherical constructs, become similar. Such diameters represent, however, incomplete assessments of fit, because they neglect matters of shape essential for effective van der Waals contacts. These geometric descriptors are replaced here by van der Waals interaction energies (E_{vdw}) determined by statistical sampling of the void space in each framework using representative DFT-derived carbocation structures. These E_{vdw} values are similar for the transition states that mediate primary and secondary isomerization and secondary β-scission reactions within each given void environment, leading to intrinsic selectivities that cannot depend on confinement effects. The marked differences in selectivity among aluminosilicates frameworks reflect instead diffusional enhancements of secondary transformations. Primary methylhexene isomers, which are more reactive and diffuse more slowly than n-heptenes, isomerize to dimethylpentenes as they egress from zeolite crystals before hydrogenating at the extracrystalline Pt function, and dimethylpentenes represent the predominant precursors to β-scission products. These diffusional effects are strongest for small voids, because they impose the most effective confinement and the most severe diffusional hurdles, and among these, on larger acid domains at higher proton densities. Reaction-transport formalisms show that Thiele moduli for these systems accurately describe selectivities with rate constants for β-scission and primary and secondary isomerization events affected similarly by a given framework, consistent with the similar E_{vdw} values for their respective transition states. The effects of intracrystalline density of accessible protons within acid domains, varied systematically as pre-adsorbed NH$_3$ titrants desorbed, on selectivities confirm these mechanistic interpretations. These data show that void structures affect selectivity, but not because of preferential stabilization of some transition states or of acid sites that vary in strength among aluminosilicate framework, as proposed previously to account for such effects. The conceptual and mathematical framework developed and used here for n-heptane isomerization on bifunctional metal-acid catalysts is general; it is also essential for rigorous mechanistic and practical assessments of catalysis on microporous catalysts, for which diffusive and confinement properties are in fact inseparable.

© 2018 Published by Elsevier Inc.

---

* Corresponding author.
   E-mail address: iglesia@berkeley.edu (E. Iglesia).

1. Introduction

Hydrocracking and hydroisomerization reactions of alkanes form shorter and more highly-branched chains with improved combustion [1] and low-temperature flow [2] properties essential for their use as fuels and lubricants. These reactions occur on microporous or mesoporous solid acids via kinetic cascades mediated by reactive alkene intermediates [3,4] and thus require a metal function to dehydrogenate alkane reactants and to scavenge reactive alkene products before they undergo undesired secondary transformations. The metal function must be sufficient in reactivity and in proximity to the acid function in order to maintain equilibrium concentrations of reactant-derived alkenes at all acid sites, a condition denoted as sufficient "intimacy" [5,6] and a requirement for reaction turnover rates to reflect the intrinsic reactive properties of the acid function. Acid strength and solvation by confinement are two such properties afforded by zeolites and zeotypes in their acid forms and essential for their catalytic function. Acid sites in zeolites with different crystalline frameworks exhibit similar acid strength [7]; they reside, however, within channels and cages of diverse structure, which stabilize to different extents confined intermediates and transition states through van der Waals contacts between the organic guests and the inorganic hosts [8–11], thus conferring, in turn, the ubiquitous diverse reactivities.

Turnover rates and product selectivities on kinetically-controlled bifunctional catalysts reflect, only in part, these confining interactions imposed by microporous solid acids. The same small pores and apertures that enhance the intrinsic reactivity of confined protons can also impede molecular diffusion in a manner that depends sensitively on the size and skeletal structure of reactant and product molecules [12,13]. Such reactant and product shape-selectivity, together with the high reactivity conferred onto protons by confinement, often leads to diffusional enhancements of secondary reactions [14,15]. The selectivity to secondary products remains non-zero even at very short bed residence times, because these products form during one sojourn within an acid domain, which is defined as the contiguous region of acid sites that separates the domains that contain the metal function. Consequently, rigorous mechanistic treatments of selectivity for these systems require reaction-transport formalisms. In their absence, the consequences of aluminosilicate framework structure for isomerization and β-scission rates have been attributed, unconvincingly and often inaccurately, to transition state selectivity [16–18] or to effects of the aluminosilicate framework structure on acid strength [19–22].

Here, we report and mechanistically interpret rate and selectivity data for the isomerization and β-scission of n-heptane on physical mixtures of Pt/SiO_2 with mesoporous or microporous aluminosilicates of different void topologies (Al-MCM-41, FAU, SFH, BEA, MFI). The use of physical mixtures allows a precise definition of the size and diffusive properties of acid domains, which are given in these systems by those of aluminosilicate crystallites. Such a strategy allows the rigorous assessment of the catalytic consequences of the void structures that confine Brønsted acid sites of similar strength within aluminosilicate frameworks [7]. n-Heptane isomerization turnover rates (per accessible proton) provide rigorous reactivity comparisons among these aluminosilicates and allow the benchmarking of reactivities derived from experiments and from density functional theory. Measured first-order isomerization rate constants increase as van der Waals interactions strengthen. These interactions are described here using energy estimates (E_{vdw}) derived from Lennard-Jones potentials and statistical sampling of the void space; they reflect the "fit" between the shape and size of the void and of the organic moiety at the transition state, in this case, a carbocation derived from the alkene reactants.

The carbocations at the ion-pair transition states that mediate primary isomerization of heptenes and secondary isomerization and β-scission of isomer alkene products are nearly identical in their "fit" within a given confining void, as expected from their similar size. As a result, these transition states are stabilized to similar extents by each given inorganic framework, leading to selectivities that should not depend on the nature of the confining voids. Measured selectivities to secondary β-scission products, however, are highest on aluminosilicates with the strongest confinement effects and, among those, on catalysts with higher proton densities and larger crystallites. Such selectivities include contributions from primary products formed during a single sojourn at an acid site and from diffusional enhancements of secondary reactions within a zeolite crystallite; these secondary reactions convert alkene products that are more reactive [14] and diffuse more slowly [23] than the linear heptene reactants as they egress from acid domains. Diffusion-reaction formalisms show that effective intracrystalline residence times, which reflect diffusional constraints of reactive product alkenes within acid domains, describe product selectivities measured on all zeolite frameworks; they demonstrate that intrinsic product selectivities are similar on all aluminosilicates, irrespective of their void structure. These measured selectivities do not reflect transition state shape selectivity or differences in acid strength among frameworks but merely the diffusional constraints imposed by small pores and voids on our ability to detect primary products.

The rigorous descriptors of reactivity and selectivity detailed herein, taken together with the experimental and computational approaches used in developing them, provide the appropriate conceptual and quantitative framework to design catalyst architectures that impose specific selectivities through the control of void and window sizes, not only for heptane reactions but also for other reactions relevant to the upgrading of diverse chemical feedstocks.

2. Methods and materials

2.1. Catalyst preparation and characterization

Mesoporous and microporous aluminosilicates (Table 1; nomenclature uses the International Zeolite Association three-letter code [27], followed by an integer distinguishing different samples with the same framework) were obtained in their proton (H^+) or ammonium (NH_4^+) forms from commercial sources (Al-MCM-41 (Sigma-Aldrich); MFI-2, MFI-3, MFI-4, and MFI-7 (Zeolyst); BEA (Zeolyst)), prepared according to previously described protocols (FAU [24], SFH [9]), or synthesized using the procedures described below (MFI-1, MFI-5, MFI-6). These latter three MFI samples were synthesized using different methods intended to obtain different crystallite sizes but with similar Si/Al ratios. MFI-1 was prepared by combining $Al_2(SO_4)_3 \cdot 18H_2O$ (51.4% wt. $Al_2(SO_4)_3$, Mallinckrodt Chemical, 0.033 g), deionized water (6.33 g), $Si(OC_2H_5)_4$ (98%, Sigma, 1.04 g), and $(C_{22}H_{45}\text{-}N^+(CH_3)_2\text{-}C_6H_{12}\text{-}N^+(CH_3)_2\text{-}C_6H_{13})Br_2$ ($C_{22\text{-}6\text{-}6}Br_2$) [25] (8.4% wt., Sachem Inc., 5.36 g) in a Teflon-lined autoclave reactor (Parr, 23 cm^3; 43/60 Hz) held at 423 K for 12 days. MFI-5 was synthesized by combining $Na_2O(SiO_2)_x \cdot xH_2O$ (9% wt. Na_2O, 28% wt. SiO_2, Fisher, 214.5 g), $(CH_3CH_2CH_2)_4N(Br)$ (98%, Fluka, 0.16 mol), $Al_2(SO_4)_3 \cdot 16H_2O$ (54.3% wt., Mallinckrodt Chemical, 6.3 g), H_2SO_4 (17.4 g), and deionized water (492 g), with sufficient NaOH (Fisher) to adjust the initial pH value to 10.5, in a plastic-lined resin kettle (Glas-Col, 1000 cm^3), held statically at 373 K for 10 days. MFI-6 was synthesized by dissolving amorphous SiO_2 (96% SiO_2, CAB-O-SIL M-5, 9 g) in a slurry containing deionized water (50 g), $(CH_3CH_2CH_2)_4N(OH)$ (40% wt., Aldrich, 12.5 g), KOH (Fisher, 1 M, 25 g), and $Al(OH)_3$

Table 1
Mesoporous aluminosilicates and zeolites.

Acid	Provenance	d_{LCS} / nm[a]	Pore env.[b]	Si/Al[c]	H$^+$/Al	R^2/D_{22DMB} / ks[g]
Al-MCM-41	Sigma-Aldrich	2.50	Mesopore	37.8	0.36[d]	≪0.09[h]
FAU	[24]	1.12	Supercage	7.5	0.39[d]	3.24 (±0.004)
SFH-1	[9]	0.763	14-MR	75.8	0.89[e]	16.8 (±1.2)
SFH-2	[9]	0.763	14-MR	45.0	0.71[e]	16.8 (±1.3)
BEA-1	Zeolyst	0.668	12-MR	11.8	0.27[d]	5.57 (±0.39)
BEA-2	Zeolyst	0.668	12-MR	43.3	0.37[e,f]	10.5 (±0.9)
MFI-1	This work	0.636	10-MR	45.1	0.32[e]	0.39 (±0.05)
MFI-2	Zeolyst	0.636	10-MR	29.2	0.64[e]	8.00 (±0.42)
MFI-3	Zeolyst	0.636	10-MR	43.8	0.89[e]	6.00 (±0.04)
MFI-4	Zeolyst	0.636	10-MR	165.8	0.62[e]	13.0 (±0.03)
MFI-5	This work	0.636	10-MR	38.9	1.19[e]	1.30 (±0.14)
MFI-6	This work	0.636	10-MR	35.0	0.65[e]	18.5 (±0.8)
MFI-7	Zeolyst	0.636	10-MR	16.6	0.77[e]	14.9 (±2.1)

[a] Diameter of the largest contained sphere for each structure [27].
[b] The pore environment for each aluminosilicate (MR indicates "membered-ring").
[c] Elemental analysis (ICP-OES; Galbraith Laboratories).
[d] From 2,6-di-*tert*-butylpyridine titration during n-heptane isomerization at 548 K (Section 2.2).
[e] From the amount of NH$_3$ evolved from heating of NH$_4^+$-exchanged samples (Section 2.1).
[f] Only peak at 673 K quantified (S1, SI).
[g] From transient uptake measurements of 2,2-dimethylbutane at 448 K (Section 2.3).
[h] The value corresponding to the fastest transient that can be regressed to the form of Eq. (5).

(53% Al$_2$O$_3$, Reheis F-2000 dried gel, 0.75 g) into a Teflon liner held within an autoclave reactor (Parr, 125 cm^3), held statically at 423 K for 10 days. Samples were filtered, washed with deionized water until the filtrate conductivity was <50 S/m, and dried under vacuum at ambient temperature for 12 h.

All samples were treated in flowing dry air (2.5 cm^3 g^{-1} s^{-1}, extra dry, Praxair) at 823 K (0.0167 K s^{-1}, 4 h at 823 K). Air-treated zeolites were exchanged three times with NH$_4^+$ using aqueous 0.1 M NH$_4$NO$_3$ (>98%, Sigma-Aldrich; 300 g solution [g zeolite]$^{-1}$). Solids were filtered and washed with deionized water (resistivity > 17.6 Ω cm^{-2}; 1500 g [g zeolite]$^{-1}$).

The elemental composition of each sample (Si, Al, Na) was determined by inductively-coupled plasma optical emission spectroscopy (Galbraith Laboratories). The number of accessible protons in Al-MCM-41, FAU, and BEA was measured by titration with 2,6-di-*tert*-butylpyridine (DTBP) during n-heptane isomerization reactions, as described in Section 2.2. The number of protons in BEA, SFH, and MFI was determined from the amount of NH$_3$ evolved during rapid heating (0.833 K s^{-1} to 823 K, 1 h at 823 K) of NH$_4^+$-exchanged zeolite samples (0.04–0.07 g); these samples were held on a coarse quartz frit within a tubular quartz reactor (7.0 mm i.d.) and treated in a mixture of He (2.5 cm^3 g^{-1} s^{-1}, 99.999% Praxair) and Ar (0.83 cm^3 g^{-1} s^{-1}, 99.999% Praxair, used as an internal standard). NH$_3$ concentrations in the effluent were measured by on-line mass spectrometry (MKS Spectra Minilab). NH$_3$ evolution profiles for NH$_4^+$-BEA-2 had two distinct peaks (S1, SI), unlike profiles for any other NH$_4^+$-zeolite. BEA samples were further characterized by ^{27}Al MAS NMR (Bruker Avance 500 MHz spectrometer in a wide-bore 11.7 Tesla magnet). Micropore volumes were measured using N$_2$ and CO$_2$ physisorption measurements (77 K and 273 K, respectively; Micromeritics 3Flex). The results of these characterizations and a discussion of the site count for BEA-2 (determined from the low temperature peak; 673 K), are included in the SI (S1).

The Pt/SiO$_2$ (2% wt.) co-catalyst was prepared by incipient wetness impregnation of SiO$_2$ [Sigma-Aldrich, Davisil Grade 646; 280 m^2 g^{-1}, 0.57 cm^3 g^{-1} pore volume; treated prior to use in 2.5 cm^3 g^{-1} s^{-1} air, extra dry Praxair at 923 K (0.083 K s^{-1}, 5 h at 923 K)] with aqueous H$_2$PtCl$_6$·6(H$_2$O) (Aldrich). The impregnated sample was treated in stagnant ambient air at 383 K for 10 h before treatment in flowing air (2.5 cm^3 g^{-1} s^{-1}, extra dry Praxair) at 823 K (0.083 K s^{-1}, 2 h at 823 K) then at 923 K (0.083 K s^{-1}, 3 h at 923 K). The sample was then treated in flowing H$_2$ (0.2 cm^3 g^{-1} s^{-1},

99.999% Praxair) at 573 K (0.083 K s^{-1}, 2 h at 573 K). The Pt dispersion (88%) was determined from total H$_2$ uptakes (assuming 1:1H: Pt$_s$ stoichiometry, where Pt$_s$ is the number of Pt surface atoms) at 373 K.

NH$_4^+$-zeolites and Pt/SiO$_2$ were mixed thoroughly using a mortar and pestle and pressed into wafers (Carver Bench Top Manual Press, 8000 psi), which were then crushed and sieved to retain 125–180 μm aggregates. These mixtures are denoted hereafter by the identity of their acid function using the notation in Table 1 (e.g., MFI-3 for a physical mixture of Pt/SiO$_2$ with MFI-3). They are also identified by their Pt$_s$/H$^+$ ratio, where Pt$_s$ was obtained from chemisorption uptakes and the H$^+$ values are those provided in Table 1.

2.2. n-Heptane isomerization and β-scission rate measurements

Rates of *n*-heptane isomerization and *β*-scission were measured at 548 K at differential conversions (<10%) on all samples (0.050–0.150 g) using a tubular reactor (316 S.S., 12 mm i.d.) with plug-flow hydrodynamics. Temperatures were maintained with a three-zone resistively heated furnace (Applied Test Systems Series 3210) using electronic controllers (Watlow, EZ-ZONE PM Series) and measured with a K-type thermocouple held within an axial thermowell at the mid-point of the packed bed. Samples were treated in 10% H$_2$/He flow (0.83 cm^3 s^{-1}; 99.999% Praxair H$_2$; 99.999% Praxair He) at 573 K (0.083 K s^{-1}) for 2 h before cooling to reaction temperature. *n*-Heptane (nC$_7$; >99.5%, Acros Organics; used as received) was introduced as a liquid using a syringe pump (Cole-Parmer 780200C series) into a flowing mixture of H$_2$ (99.999% Praxair) and He (99.999% Praxair) in heated transfer lines (>423 K) to prevent reactant condensation. Alkane and H$_2$ concentrations were varied independently (60–100 kPa H$_2$; 6–300 H$_2$/alkane molar ratio) by metering liquid and gas flow rates. Reactant and product concentrations in the reactant and effluent streams were measured by on-line gas chromatography (Agilent 6890N GC) using a methyl silicone capillary column (Agilent HP-1; 50 m × 0.32 mm × 1.05 μm) and flame ionization detection.

The number of accessible protons was measured during catalysis on mesoporous aluminosilicates and three-dimensional large-pore zeolites (Al-MCM-41, FAU, BEA) by titration with 2,6-di-*tert*-butylpyridine (DTBP; >97%, Sigma-Aldrich; used as received), which selectively interacts with Brønsted acid sites [26]. Bulky DTBP titrants cannot diffuse through the one-dimensional channels of

SFH or into the 10-MR channels of MFI. The accessibility of DTBP to confined protons in BEA, whose channels are only slightly larger than those of MFI (6 Å vs. 4.7 Å [27]), was confirmed by CHN analysis (Carlo-Erba Combustion Elemental Analyzer; S1, SI) of DTBP-treated (0.48 Pa DTBP vaporized into a flowing H_2/He stream for 4 h, followed by flowing H_2/He for 0.5 h to remove weakly adsorbed titrant) BEA-1, BEA-2, and MFI-3, where MFI-3 represents the comparison case. For titration during reaction, DTBP was dissolved in the liquid n-heptane reactant ($2.2–9.6 \times 10^{-4}$ mol fraction) and vaporized into a flowing H_2/He stream (0.11–0.48 Pa DTBP). Isomerization and β-scission rates and DTBP uptakes were calculated from the effluent concentrations of the reactant, products, and titrant. The number of DTBP molecules required to fully suppress rates (assuming 1:1 DTBP:H^+ stoichiometry) was determined by titrant uptake as isomerization and β-scission rates decreased to zero (titration plots for Al-MCM-41, FAU, and BEA in S2, SI). The complete suppression of isomerization and β-scission reactivity upon saturation DTBP uptakes for Al-MCM-41, FAU, and BEA-1 indicates that Lewis acid sites, present in these samples as extraframework Al species, do not contribute detectably to measured rates. BEA-2 rates cannot be fully suppressed (10% residual rates), because the ubiquitous stacking faults in BEA [28,29] impede DTBP access to some regions within crystallites. The evidence for these conclusions and a discussion of BEA-2 proton counts are included in the SI (S1).

Rates are reported here as turnover rates, normalized by the number of H^+ in each sample (Table 1). Turnover rates were corrected for approach to equilibrium ($\eta_{j,i}$) for the conversion of the reactants (react) to each isomer product (prod):

$$r_{forward} = r_{net} \left(1 - \eta_{prod,react} \right)^{-1} \tag{1}$$

where the approach to equilibrium ($\eta_{j,i}$) for species i to species j is defined as:

$$\eta_{j,i} = \left(\frac{P_j}{P_i} \right) K_{j,i}^{-1} \tag{2}$$

(P_j/P_i) is the molar (pressure) ratio of species j to species i and $K_{j,i}$ is the equilibrium constant calculated at 548 K from tabulated thermodynamic data [30,31] for each i-j pair. Measured β-scission products remained far from equilibrium ($\eta < 10^{-4}$) at all conditions. Rates were measured periodically at a reference condition (100 kPa H_2, 0.5 kPa alkane) to detect (and correct for) any intervening deactivation; only minor deactivation was detected (<10% change after 60 h) and predominantly at low H_2/n-heptane ratios.

Measured (fractional; S_j) and intrinsic ($S_{j,0}$) selectivities are defined as:

$$S_j = \frac{r_j}{\sum_j r_j} \tag{3}$$

$$S_{j,0} = \frac{r_{j,0}}{\sum_j r_{j,0}} \tag{4}$$

where r_j is the measured formation rate of each product from reactant n-heptane, and the subscript "0" refers to the product formation rates resulting from single sojourns at active sites (as discussed in detail in Sections 3.2 and 3.4). All reported uncertainties for rate constants and selectivities reflect 95% confidence intervals.

2.2.1. n-Heptane isomerization and β-scission rate measurements during desorption of reversibly-bound titrants of acid sites

Product selectivities (S_{prod}) were measured during transient desorption of NH_3, a titrant reversibly bound at 548 K, in order to assess intrinsic primary values ($S_{prod,0}$, defined in Eq. (4); as

discussed in Section 3.4) and the diffusional enhancements of secondary reactions. Such titrant desorption events gradually and monotonically increase intracrystalline residence times for products and thus the extent to which their subsequent reactions contribute to measured selectivities by increasing the intracrystalline density of accessible protons. Intrinsic selectivities were obtained by extrapolating measured selectivities to their values at the point of nearly full proton titration, because low proton densities minimize product readsorption and interconversion events within a given crystallite.

These experiments were performed by treating samples as described above and then exposing them to a stream containing 0.5 kPa NH_3 (0.83 cm^3 s^{-1}, 1% NH_3 in He, Praxair; diluted with He, 99.999% Praxair) for 2 h. Isomerization and β-scission rates and selectivities (100 kPa H_2; H_2/alkane = 200) were then measured periodically after removing the titrant from the gaseous stream and as the adsorbed titrants gradually desorbed. Reaction rates and selectivities after 15 ks returned to 95%-100% of their values before exposure to NH_3 for most samples, indicating the complete desorption of the titrant. Rates and selectivities on BEA-1, MFI-6, and MFI-7 returned to 75%-80% after 15 ks because of intervening catalyst deactivation.

2.3. Diffusional properties of solid acids from transient 2,2-dimethylbutane uptakes

The relevant diffusion distances in bifunctional mixtures are defined by the zeolite crystallite size, because interstices among aluminosilicate crystals and within Pt/SiO_2 aggregates are much larger and consequently impose much less severe diffusional hurdles [6]. Zeolite crystallite sizes are typically inferred visually from electron micrographs, a method that becomes inaccurate for crystallites that are irregular in shape or distributed in size. These visual methods fail to detect the twinning or misaligned intergrowths [32] that impairs intracrystalline diffusion. Here, characteristic diffusion times (R^2/D (units: s), where R is the effective crystallite radius and D is the diffusivity) are used to assess the extent of reactant (Section 3.1) and product (Section 3.4) intracrystalline diffusional constraints. These R^2/D values are used as a proxy for the effective crystallite size among acids of a given framework, because the molecular diffusivity of the probe sorbate is a unique characteristic of each given zeolite framework [23].

These R^2/D values were determined for each sample using transient uptake measurements of 2,2-dimethylbutane (22DMB; >98% purity, Sigma-Aldrich, purified by three freeze-pump-thaw cycles) at 448 K in a constant volume apparatus (schematic diagram in S3, SI). NH_4^+-zeolites (~0.10 g) were treated in flowing 5% O_2/He mixture (8.3 cm^3 g^{-1} s^{-1}, 99.999% Praxair) at 723 K (0.025 K s^{-1}) for 2 h before measurements. Samples were evacuated to < 0.1 Pa for 1.5 h and cooled to 448 K then isolated from the manifold, in which an initial 22DMB pressure of 0.6 kPa was established. The manifold and sample were then reconnected, and uptake transients were measured (with millisecond resolution) using a pressure transducer (MKS Baratron Type D28B Dual-Range Manometer) until constant pressures were attained. The sorbate pressure was then increased (by ~0.5 kPa 22DMB), and each subsequent uptake transient was measured. 22DMB pressures were systematically increased from 0.6 to 4.0 kPa in steps of 0.5 kPa. The experimental apparatus was designed to keep nearly constant pressure (<10% change) during each transient. Transient uptakes in systems with these small changes in pressure can be accurately described by an equation that describes diffusion processes characterized by a concentration-independent diffusivity (D) for quasi-spherical diffusion domains of nearly uniform radius, R [33]:

$$\frac{M_t}{M_\infty} = 1 - \frac{6}{\pi^2} \sum_{n=1}^{\infty} \frac{1}{n^2} \exp\left(\frac{-D\pi^2 n^2 t}{R^2}\right) \tag{5}$$

where M_t is the molar uptake at time t and M_∞ that at equilibrium. Regression of measured transients to Equation (5) yielded R^2/D values.

Accounting for a Gaussian distribution in crystallite size improved regressed fits without concomitant variations in R^2/D values (discussed in S4, SI). The thermodynamically non-ideal character of solutes within zeolites [34] and the consequent effects of intracrystalline concentrations on diffusivities were taken into account by correcting measured R^2/D values using the Darken equation [12]:

$$D_0 = D\left(\frac{d\ln(q)}{d\ln(P)}\right) \tag{6}$$

($d\ln(q)/d\ln(P)$) values (q is the adsorbed-phase concentration and P is pressure) were obtained from measured equilibrium uptake isotherms. Values of R^2/D_{22DMB} (R^2/D for 22DMB; corrected by Eq. (6)) are included in Table 1. The fast uptake transients for Al-MCM-41 were shorter than the temporal resolution of the pressure transducer (~1 ms); the R^2/D_{22DMB} value reported therefore represents a lower bound.

2.4. Density functional theory (DFT) methods

The energies of transition states and relevant precursors were calculated using periodic plane-wave density functional theory (DFT), as implemented in the Vienna *ab initio* simulation package (VASP 5.3.5) [35–38]. The basis set of Bloch waves was truncated at 396 eV. The revised Perdew-Burke-Ernzerhof (RPBE) functional within the generalized gradient approximation (GGA) was used to describe exchange and correlation energies [39,40]. The projector augmented wave method (PAW5) was used to account for interactions between valence and core electrons [41,42]. Empirical dispersive energy corrections (DFT-D3) with Becke-Johnson (BJ) damping [43,44] were incorporated at each structure and energy optimization step in order to account for van der Waals interactions. The first Brillouin zone was sampled using a $(1 \times 1 \times 1)$ Γ-centered k-point mesh. Electronic structures were relaxed until the energy difference between iteration steps was $<1 \times 10^{-6}$ eV and forces on all atoms were <0.05 eV Å^{-1}.

MFI unit cells were constructed using orthorhombic unit cell parameters (2.0022 nm × 1.9899 nm × 1.3383 nm, α = β = γ = 90°; used without relaxation) and atomic coordinates from X-ray crystallography [45]; framework atoms were numbered according to the convention of Olson [46]. Brønsted acid sites (1 H$^+$/unit cell (u.c.), corresponding to a Si/Al of 95) were generated by substituting Si^{4+} with Al^{3+} at the T-12 site and placing a proton at the O-20 site to balance the resultant framework charge. This site lies at the intersection of MFI straight and sinusoidal channels; an image of the location of this site within MFI is included in the SI (S5). Ten of the twelve crystallographically unique T-sites in MFI allow protons to face into such intersections, and Al atoms preferentially reside at such locations for the Si/Al ratios in most of the MFI samples used here [47] (as discussed in Section 3.3).

Transition state structures and energies were obtained by calculating minimum energy paths using nudged elastic band (NEB) methods [48] with individual structures converged to within 1×10^{-4} eV (energy) and <0.3 eV Å^{-1} total forces at each atom. Transition state structures were refined using the Henkelman dimer method [49] with convergence criteria of 1×10^{-6} eV for energy and 0.05 eV Å^{-1} for forces. Löwdin population analyses [50] were used to obtain charge distributions for converged structures after transforming wavefunctions into localized quasiatomic orbitals (QUAMBO) [51–54]. Converged transition state structures,

extracted from their confining void for visual clarity, are included in the SI (S6).

Transition state (TS) carbocation volumes (V) and surface areas (A_s) were obtained from Connolly surfaces [55] using a solvent radius of 1.4 Å; sizes of each transition state carbocation (TS carbocation) are reported here using two definitions that represent a range of characteristic diameters as those of the sphere of equivalent volume ($d_{eq} = 6V/A_s$) and of equivalent surface area ($d_{eq,SA} = \sqrt{A_s/\pi}$). These TS carbocations, however, are not spherical; their nonsphericity index (v) is given by $v = d_{ch}/d_{eq}$, the ratio of the longest chord within the carbocation (d_{ch}) to d_{eq}. The distance between the center of charge in the TS carbocation and the conjugate anion (l_{cs}) were also calculated. These values (d_{eq}, $d_{eq,SA}$, v, and l_{cs}) are listed in Table 3 for the TS structures examined in this study.

Zero-point vibrational energies (ZPVE), vibrational enthalpies and free energies (H_{vib}, G_{vib}, respectively) for all structures, and translational and rotational enthalpies and free energies (H_{trans}, H_{rot}, G_{trans}, G_{rot}) for gaseous molecules were determined from frequency calculations performed on optimized structures. Enthalpy and free energy were then calculated by adding corrections to DFT-derived electronic energies (E_0) and dispersive corrections (E_{D3-BJ}):

$$H = E_0 + E_{D3-BJ} + ZPVE + H_{vib} + H_{trans} + H_{rot} \tag{7}$$

$$G = E_0 + E_{D3-BJ} + ZPVE + G_{vib} + G_{trans} + G_{rot} \tag{8}$$

Low-frequency vibrational modes (<110 cm^{-1}) resemble hindered translations and rotations and are inaccurate in these calculations. Yet, they contribute significantly to vibrational free energy estimates; as a result, they were replaced by a fraction (0.70) of the translational and rotational free energies of their respective gaseous analogs, as proposed previously [56].

Each species formed along the reaction coordinate consists of an ensemble of energetically accessible configurations, which includes, for instance, all their conformational isomers. These ensembles include configurations which are quasi-equilibrated in kinetic analysis, as discussed in Section 3.2; specifically, the ensemble of linear heptenes ($nC_7^=$) contains all heptene regioisomers and the ensemble of heptene-derived alkoxides (nC_7^*) contains all heptoxides with different attachment points to the zeolite framework (the specific configurations composing each ensemble, $nC_7^=$ and nC_7^*, are depicted in Scheme 3a). Transition state ensembles contain all individual transition states that convert all alkoxides derived from a given alkene to alkoxides from an alkene with a different skeletal backbone, because each of these transition state configurations contributes to experimentally measured rates and intrinsic selectivities. For example, the transition states converting a specific nC_7^* to a specific 2-methylhexoxide (2MH*) and converting a different nC_7^* to a 2MH* with a different attachment point to the zeolite framework both contribute to measured rates and selectivities as nC_7 to 2MH isomerization events.

Gibbs free energies evaluated for each ensemble m ($\langle G^m \rangle$), composed of n configurations (each with free energy, G_n^m):

$$\langle G^m \rangle = -k_B T \ln\left(\sum_n \exp\left(\frac{-G_n^m}{k_B T}\right)\right) \tag{9}$$

where k_B is the Boltzmann constant and T is temperature, permit rigorous comparisons with experiment. Free energy barriers ($\langle \Delta G^\ddagger \rangle$) were evaluated from the free energies of a given ensemble of transition states ($\langle G^\ddagger \rangle$) and their relevant precursors ($\langle G^{ref} \rangle$):

$$\langle \Delta G^\ddagger \rangle = \langle G^\ddagger \rangle - \sum_{ref} \langle G^{ref} \rangle \tag{10}$$

2.4.1. Algorithms for evaluating van der Waals interaction energies

One-dimensional geometric descriptors of size for TS carbocation and inorganic voids, such as the diameter of equivalent spheres, neglect their diverse shapes. Interactions between confined structures and inorganic hosts are more accurately described using Lennard-Jones potentials to estimate van der Waals interaction energies (E_{vdw}). Structures for TS carbocation optimized at the MFI T12 site were placed at each crystallographically unique T-site in MFI and in other zeolite frameworks (FAU, SFH, BEA) using previously described methods and algorithms [10]. The charge separation at the TS (the distance between the center of charge in the TS carbocation and the conjugate anion, l_{cs} in Table 3) was determined from the TS structure optimized in MFI and was held constant because van der Waals interactions were determined to have only minor effects on this distance for a series of transition states mediating the conversion of C_4–C_7 linear-alkenes to mono-branched-alkenes, which differ significantly in size, at MFI Al12-O20(H) (as discussed in S7, SI). Atomic coordinates and unit cell parameters for FAU (2.4345 nm × 2.4345 nm × 2.4345 nm, $\alpha = \beta = \gamma = 90°$); SFH (0.5255 nm × 3.4319 nm × 2.1518 nm, $\alpha = \beta = \gamma = 90°$); and BEA (1.2632 nm × 1.2632 nm × 2.6186 nm, $\alpha = \beta = \gamma = 90°$) were taken from the International Zeolite Association database [27] and used without relaxation. Supercells were constructed to fully enclose confined species at each accessible T-site (e.g., SFH 3 × 1 × 1, BEA 3 × 2 × 2) in order to accurately determine van der Waals interaction energies using Lennard-Jones potentials:

$$E_{vdw} = \varepsilon \sum_a \sum_b \left(\left(\frac{d_{a,b}}{d_{a,b,eq}} \right)^{-12} - 2\left(\frac{d_{a,b}}{d_{a,b,eq}} \right)^{-6} \right) \quad (11)$$

where a is the index for framework oxygen atoms, b is the index for atoms in the TS carbocation, $d_{a,b}$ is the distance between the a-b pair, $d_{a,b,eq}$ is the equilibrium distance for each a-b pair and is defined here as the sum of their van der Waals radii [57], and ε is a scaling parameter determined by benchmarking E_{vdw} values against those derived from empirical dispersive corrections in periodic DFT calculations ($E_{D3\text{-}BJ}$ in Eqs. (7) and (8)) in previous work ($\varepsilon = 1.59$ kJ mol^{-1}) [10]. Any a-b pairs present within covalent interaction distances ($d_{a,b} < 0.15$ nm) are neglected because their pairwise interaction energies are predominantly the result of such covalent bonds. Values of E_{vdw} were weighted by the probability of each orientation (subscript n) at each framework T-site to obtain interaction energies for each T-site ($\langle E_{vdw} \rangle_T$):

$$\langle E_{vdw} \rangle_T = -k_B T \ln \left(\sum_n \exp\left(\frac{-E_{vdw,n}}{k_B T} \right) \right) \quad (12)$$

Interaction energies ($\langle E_{vdw} \rangle$) relevant for reactivity were determined by weighting $\langle E_{vdw} \rangle_T$ by their probability of occurring, assuming random Al distribution for FAU, SFH, and BEA by accounting for all T-sites. For MFI, such interaction energies were evaluated assuming the random Al distribution throughout but also by taking only the values for carbocation locations within MFI intersections (as discussed in Section 3.3).

$$\langle E_{vdw} \rangle = -k_B T \ln \left(\sum_T \exp\left(\frac{-\langle E_{vdw} \rangle_T}{k_B T} \right) \right) \quad (13)$$

These $\langle E_{vdw} \rangle$ values (Eq. (13)) represent the interaction energy that a given transition state carbocation feels within each specific zeolite framework (or, in the case of MFI, for samples with Al preferentially placed in intersections and randomly distributed throughout the framework). Values of $\langle E_{vdw} \rangle_T$ and $\langle E_{vdw} \rangle$ are evaluated for a representative transition state structure within each ensemble of TS structures that all contribute to convert alkenes of one backbone to alkenes of another backbone (as discussed in Section 2.4); this representative structure is given by that with

the smallest free energy from DFT, because this specific TS contributes most significantly to the free energy of the TS ensemble (Eq. (9)).

3. Results and discussion

3.1. Site proximity requirements for n-heptane isomerization and β-scission on bifunctional catalysts

n-Heptane (nC$_7$) isomerization and β-scission rates and selectivities were measured on mesoporous and microporous aluminosilicates with diverse void structures (Al-MCM-41, FAU, SFH, BEA, MFI) (Table 1), present in physical mixture with Pt/SiO$_2$. Measured isomerization and β-scission rates (per mass) were much larger (by >10^3-fold) on bifunctional mixtures than on either monofunctional component alone, as expected from the required formation of alkene intermediates for acid-catalyzed isomerization events. Alkene transformations on Brønsted acid sites limit isomerization rates for sufficiently intimate bifunctional mixtures [4]. Such intimacy is defined by the presence of the same (equilibrium) alkene concentration at all sites within porous solid acid domains; this requires, in turn: (i) metal contents that are adequate to attain reactant alkane dehydrogenation equilibrium at the external surface of the acid domains and (ii) acid and metal sites that are sufficiently proximate to prevent intervening gradients in alkene concentrations within acid domains.

The equilibration of n-heptane with all linear heptene isomers (and H$_2$) on the Pt function was confirmed by similar n-heptane consumption rates on mixtures of MFI-3 and Pt/SiO$_2$ with different Pt$_s$/H$^+$ ratios (7.8 and 18; Pt$_s$ is the number of Pt surface atoms from chemisorption uptakes (Section 2.1); H$^+$ is from NH$_3$ evolved during thermal treatments of NH$_4^+$-exchanged SFH, BEA-2, and MFI (Section 2.1) or from DTBP titrations during isomerization reactions for Al-MCM-41, FAU, and BEA-1 (Section 2.2)). Fig. 1 shows nC$_7$ consumption turnover rates (per H$^+$) as a function of nC$_7$/H$_2$ reactant molar ratios, which were set by independent changes in nC$_7$ and H$_2$ pressures. Turnover rates were nearly identical for mixtures with Pt$_s$/H$^+$ ratios of 7.8 and 18; they were also a single-valued function of nC$_7$/H$_2$ reactant ratios on such mixtures. These results indicate that nC$_7$/H$_2$ reactant mixtures are present in equilibrium with all linear heptene regioisomers and that nC$_7$/H$_2$ reactant ratios therefore represent the relevant surrogate for the prevalent pressure of linear heptenes. Rates on these two mixtures increased linearly with nC$_7$/H$_2$ molar ratios at low values and became nearly constant at higher molar ratios. In contrast, rates were lower for a mixture with a 1.6 Pt$_s$/H$^+$ ratio; they could not be described solely by the prevalent nC$_7$/H$_2$ reactant ratios, consistent with a metal function that was insufficient to equilibrate hydrogenation-dehydrogenation reactions. These data show that mixtures with Pt$_s$/H$^+$ ratios larger than 8 led to the equilibration of n-heptane with all linear heptenes (and H$_2$) at extracrystalline regions where the metal function resides.

Linear heptene concentrations below equilibrium may prevail, however, within acid domains, defined here by the aluminosilicate crystallites. The presence and severity of intracrystalline heptene concentration gradients can be rigorously described by reaction-transport models for quasi-spherical domains, which lead to a Thiele modulus (ϕ_A):

$$\phi_A^2 = \frac{\alpha_1 \rho_{H^+} R^2}{D_A} \quad (14)$$

as the relevant dimensionless parameter. In Equation (14), α_1 is the first-order isomerization rate constant, D_A is the diffusivity of linear heptenes, and ρ_{H^+} is the volumetric proton density within acid
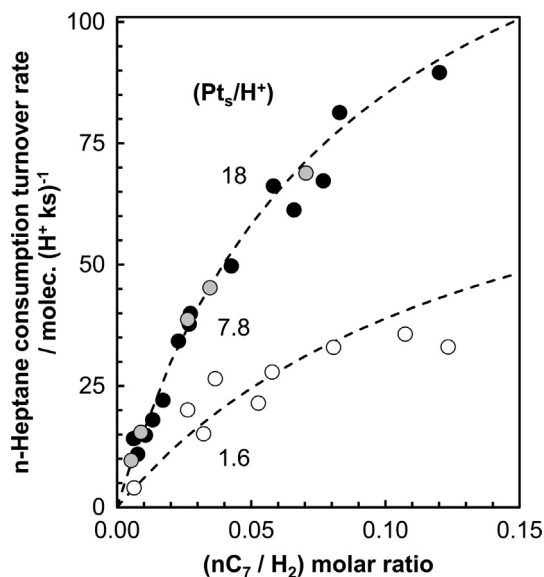
Fig. 1. *n*-Heptane consumption turnover rate (per H+) as a function of (nC7/H2) molar ratio on physical mixtures of Pt/SiO2 and MFI-3, where Pts/H+ ratio is 1.6 (white), 7.8 (gray), and 18 (black) (0.02–12 kPa nC7, 60–100 kPa H2, 548 K). Dashed curves represent regression of data to the functional form Equation (23).

domains. This Thiele modulus [58] represents the ratio of characteristic reaction to diffusion rates for heptene reactants.

Measured turnover rates reflect their strict kinetic origins for small ϕ^2 values (≤ 1), but they are influenced by intracrystalline gradients in reactant alkene concentrations as ϕ^2 increases (>1) [58]. The first-order rate constants (α_1 in Eq. (14), per proton) reflect the free energies of the relevant transition states (TS), determined for microporous solid acids by the conjugate anion stability (acid strength, similar for all aluminosilicates [7]) and by van der Waals contacts (confinement) that differ among aluminosilicate frameworks.

Confining voids influence the reactivity of protons but also molecular diffusivities, which are characteristic of a given void structure but are insensitive to crystallite size [12] or proton density [59]. Diffusivities decrease as molecular sizes approach aperture diameters [23,34]; the diffusivity of a probe sorbate can be used as a surrogate for those of linear heptenes for acids with each given framework, as long as the size of the probe sorbate does not preclude its accessing the intracrystalline void space. The diffusivities (D_{22DMB}) of 2,2-dimethylbutane (22DMB), used here as the probe molecule, were measured as R^2/D_{22DMB} values (Eq. (5); Section 2.3); these values reflect characteristic diffusion times that depend only on the crystallite radius (R) for each given framework. Thus, the presence and severity of intracrystalline concentration gradients of reactant alkenes for solids with a given void structure reflect a simplified Thiele modulus, Ξ (Ξ^2, units: s cm^{-3}):

$$\Xi^2 = \frac{\rho_{H^+} R^2}{D_{22DMB}} \tag{15}$$

which extracts the essential structural features of different aluminosilicates from its dimensionless counterpart (Eq. (14)).

The presence and kinetic consequences of intracrystalline gradients of *n*-heptenes in MFI were determined by measuring rates on physical mixtures of Pt/SiO2 with MFI samples of different Ξ^2 values (Pts/H+ > 8), varied through systematic changes in:

(i) ρ_{H^+} for samples with similar R^2/D_{22DMB} (1.09–1.24 × 10^4 s; Table 1, MFI-2, MFI-3, MFI-4);

(ii) R^2/D_{22DMB} for samples with similar ρ_{H^+} (5.53–6.5 × 10^{-4} mol cm^{-3}; MFI-2, MFI-3, MFI-6); or

(iii) both R^2/D_{22DMB} and ρ_{H^+}, in the case of MFI-1 and MFI-5 solid acids.

Fig. 2 shows that nC7 consumption turnover rates remain constant for Ξ^2 values up to 6 s cm^{-3} but decreased for larger Ξ^2 values, indicating the onset of intracrystalline *n*-heptene gradients. These data were obtained at nC7/H2 ratios (0.005 nC7/H2 ratio) that lead to linear rate dependences on *n*-heptene concentrations (Fig. 1). Any kinetic effects of concentration gradients would become less severe as rates approach zero-order kinetic dependences at higher nC7/H2 ratios and heptene concentrations. The data in Fig. 2 thus show that nC7 turnover rates on MFI samples with Ξ^2 values below 6 s cm^{-3} reflect the rates of chemical reactions at intracrystalline protons that are exposed to equilibrium linear heptene concentrations, as established at extracrystalline regions by the Pt function.

Turnover rates on mesoporous acids and on large-pore zeolites (Al-MCM-41, FAU, SFH, and BEA), which show smaller rate constants (Table 2; Section 3.3) and similar (or smaller) R^2/D_{22DMB} values (Table 1) compared with MFI, must also therefore reflect the extracrystalline equilibrium concentrations of heptenes, at least for mixtures with sufficient metal function (Pts/H+ > 8 for FAU, SFH, BEA, and MFI; Pts/H+ ∼ 2 for Al-MCM-41 because of its 200-fold lower turnover rate than for MFI; discussed in S8, SI). The rigorous kinetic origins of these measured turnover rates allow the unequivocal mechanistic interpretation of reactivity in terms of the kinetic formalisms described below.

3.2. Elementary steps for primary isomerization events and secondary β-scission reactions

This section examines the primary and secondary reactions that consume *n*-heptane via isomerization and β-scission of equilibrated linear heptenes, as well as the elementary steps that mediate such reactions. Fig. 3 shows the selectivities (Eq. (3)) and approach to equilibrium parameters ($\eta_{2MH,3MH}$, Eq. (2)) for 2-methylhexane (2MH) and 3-methylhexane (3MH) products of
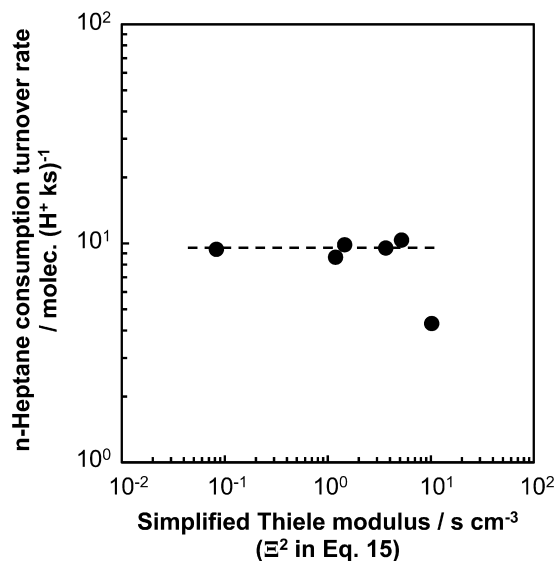

Fig. 2. *n*-Heptane consumption turnover rate (per H+) as a function of the simplified Thiele modulus (Ξ^2, Eq. (15)) on physical mixtures of Pt/SiO2 and MFI-1 – MFI-6 (Pts/H+ ∼ 7.8–9.6, 0.0048–0.0052 (nC7/H2) molar ratio, 60–100 kPa H2, 548 K). The dashed line is the average rate on samples with Ξ^2 values less than 6 s cm^{-1}.

Table 2
Rate constants for nC$_7$ isomerization (per H$^+$, 548 K), as defined in Equation (23), on mesoporous and microporous aluminosilicates.

Acid	$k_{isom,nC_7} K_{prot,nC_7}$ [a]	k_{isom,nC_7} [b]
Al-MCM-41	0.647 (±0.025)	1.80 (±0.51)
FAU	8.88 (±0.38)	46.5 (±35)
SFH-1	35.5 (±4.1)	39.9 (±10)
SFH-2	33.1 (±1.6)	47.1 (±5.7)
BEA-1	88.7 (±4.7)	80.4 (±19.4)
BEA-2	83.6 (±2.7)	74.9 (±9.9)
MFI-1	93.5 (±2.0)	112 (±15)
MFI-2	103 (±1.3)	111 (±14)
MFI-3	93.5 (±3.5)	158 (±43)
MFI-4	117 (±8.5)	108 (±34)
MFI-5	90.7 (±4.8)	96.6 (±42)
MFI-6	40.8 (±0.34) [c]	61.5 (±6.5) [c]
MFI-7	246 (±9.0) [c]	315 (±85) [c]

[a] units: (Pa H$^+$ ks)$^{-1}$.

[b] units: (H$^+$ ks)$^{-1}$.

[c] measured rate constants are corrupted by kinetically-relevant reactant concentration gradients (Section 3.1 for MFI-6, Section 3.3 for MFI-7).

nC$_7$ reactions on Al-MCM-41 as a function of the reactant conversion, varied here through changes in bed residence times. These data show that 2MH and 3MH (Fig. 3, left) form as primary products, without detectable concentrations of dimethylpentanes or β-scission products at any reactant conversions. 2MH forms initially at higher selectivities than does 3MH but undergoes subsequent facile methyl-shift isomerization to form 3MH with increasing residence times, leading to 3MH-2MH ratios that approach equilibrium values (Fig. 3, right). These selectivity trends are consistent with the quasi-equilibrated desorption of product alkoxides to form primary alkene products and with their undetectable secondary interconversion rates as they egress from Al-MCM-41 channels and hydrogenate at the extracrystalline Pt function.

Dimethylpentanes were not detected on Al-MCM-41, even at bed residence times that led to equilibrium 2MH-3MH ratios; the alkyl-substituted cyclopropyl carbenium ions [60–62] that act as the isomerization TS (together with the conjugate anion of the Brønsted acid) form and cleave C—C bonds in a concerted manner that precludes any changes in backbone length by more than a single C-atom during each isomerization event [5,14,61]. As a result, dimethylpentenes cannot form directly from linear heptenes but instead require readsorption and subsequent rearrangements of primary methylhexene products formed via quasi-equilibrated deprotonation of methylhexoxides. These secondary reactions occur much more slowly than the methyl shifts that lead to 2MH-3MH equilibration [14].

On all zeolites, but not on Al-MCM-41, 2MH and 3MH form at all bed residence times concurrently with 2,4-dimethylpentane
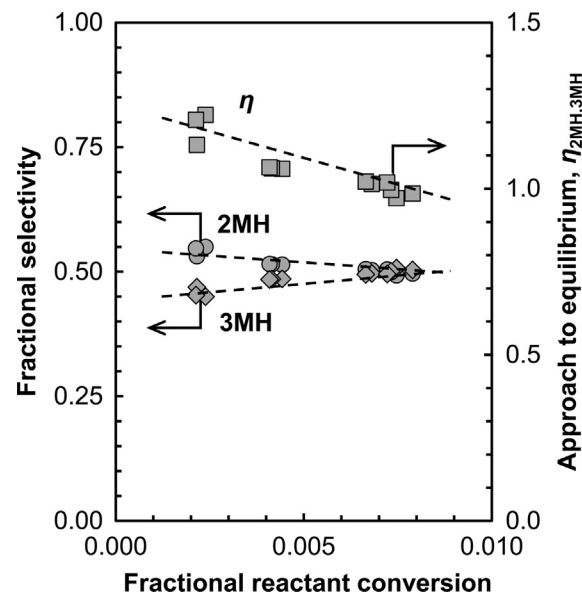

Fig. 3. Measured product selectivities for 2-methylhexane (2MH; diamonds, left) and 3-methylhexane (3MH; circles, left) and approaches to equilibrium ($\eta_{2MH,3MH}$, Eq. (2)) for 2MH/3MH (squares, right) as a function of reactant n-heptane conversion, varied by changes in reactant space velocity, during n-heptane isomerization on a physical mixture of Pt/SiO$_2$ and Al-MCM-41. 35–165 molec. (H$^+$ ks)$^{-1}$ space velocity, 0.01 nC$_7$/H$_2$ molar ratio, 100 kPa H$_2$, 548 K. The dashed lines indicate trends.

(24DMP) and with equimolar propane-isobutane mixtures derived from β-scission events. 2,3-Dimethylpentane (23DMP) was also detected along with 2,2-dimethylpentane (22DMP) and 3,3-dimethylpentane (33DMP) (<0.01 fractional selectivity for all three isomers) on large-pore FAU and SFH but not on MFI or BEA. Even at very low conversions, all product selectivities were non-zero, a characteristic of molecules that form during a single sojourn at a catalytic site. In this case, however, these non-zero initial selectivities reflect secondary interconversions that occur within an acid domain, before primary alkene isomers, which are more reactive and diffuse more slowly than the linear heptene reactants, leave a zeolite crystallite and hydrogenate at the extracrystalline Pt function. The extent to which these diffusion-enhanced secondary reactions contribute to the observed selectivities depends on the intracrystalline residence times (Eq. (29)) of the alkene products, as discussed in Section 3.4. In contrast, the larger mesopores in Al-MCM-41 (2.5 nm diameter), which contain sites similar in acid strength to these zeolites [7,63], minimize intracrystalline gradients of isoalkenes by the combined effects of faster molecular diffusion [34] and weaker confinement that lead to less reactive acid

Table 3
Sizes of representative spheres for and nonsphericity (v) of carbocations at transition states[*] for primary and secondary isomerization and β-scission reactions involved in nC$_7$ isomerization. Values represent the mean for transition state carbocations in each ensemble.

Transition state carbocation mediating	Diameter of the sphere of equivalent volume (d_{eq}) or surface area ($d_{eq,SA}$) / nm [a]		Nonsphericity index, v [b]	Charge separation, l_{cs} / nm [c]
	d_{eq}	$d_{eq,SA}$		
nC$_7$-2MH$^=$	0.636	0.698	1.51	0.401
nC$_7$-3MH$^=$	0.636	0.692	1.52	0.408
24DMP$^=$-23DMP$^=$	0.635	0.687	1.45	0.430
24DMP$^=$-β-scission	0.649	0.699	1.39	0.361

[*] Transition states were converged at MFI Al12; structures are included in S6, SI.

[a] Carbocation volume and surface area assessed from the Connolly surface [55].

[b] Unitless; v is given by the ratio of the longest chord within the carbocation to d_{eq}.

[c] The distance between the center of charge in the transition state carbocation and the conjugate anion.

sites (Section 3.3). Thus, the products observed on Al-MCM-41 (Fig. 3) reflect intrinsic single-sojourn selectivities (Eq. (4)) and the identity of the molecules formed in one reactive encounter with an acid site; secondary interconversions then occur slowly along the catalyst bed to an extent dictated by bed residence times, which, for Al-MCM-41, are longer than intracrystalline residence times.

The prevalence of singly-branched isomers and the absence of β-scission products on Al-MCM-41 have been inaccurately attributed in previous studies [19,64,65] to acid sites that are much weaker than those in zeolites and to an essential requirement for such stronger acids to favor isomerization events that change the backbone length and cleave C—C bonds over facile methyl shifts. In fact, these premises are not correct; selectivities on Al-MCM-41 and zeolites differ because larger voids and channels favor fast diffusion and low intrinsic reactivities, the latter through the effects of confinement instead of acid strength, thus minimizing diffusional enhancements of secondary interconversions. Moreover, the ratio of β-scission to isomerization rate constants, in fact, decreases with increasing acid strength; the stronger localization of positive charge in β-scission TS carbocations than in those involved in isomerization leads to weaker stabilization of β-scission TS relative to isomerization TS on stronger acids [66].

The transformation of methylhexenes to dimethylpentenes, the extent to which they equilibrate, and the identity of the precursors that undergo β-scission cannot be assessed experimentally on Al-MCM-41, because none of these secondary reaction products form. These secondary reactions become increasingly consequential as the voids in solid acids become smaller because the more effective van der Waals contacts with TS carbocations lead to higher reactivity (Section 3.3) and because of smaller intracrystalline diffusivities.

These secondary reactions are examined here using activation free energies derived from density functional theory (DFT) on MFI, the zeolite framework that provides the most effective van der Waals contacts with TS carbocations among the solid acids examined in this study. These DFT methods use functionals that account for dispersive effects at each energy and geometry optimization (Section 2.4, representative TS structures in S6, SI). The conclusions reached here for MFI remain pertinent for Al-MCM-41 and for large-pore zeolites (FAU, SFH, BEA) because the TS carbocation that mediate isomerization and β-scission events are similar in size; as a result, their energies are similarly affected by confinement within each given zeolite framework (Section 3.3).

DFT methods can isolate the many individual TS configurations that mediate the multiple routes by which one alkene (through its various alkoxide attachment isomers) can convert to a different skeletal isomer or to smaller fragments. For example, 2-methylhexene isomerization to 3-methylhexene occurs through 2-methyl-2-hexene (via 2-methylhex-3-oxide) conversion to 3-methyl-2-hexene (via 3-methylhex-2-oxide) and through 2-methyl-1-hexene (via 2-methylhex-2-oxide) conversion to 3-methyl-3-hexene (via 3-methylhex-3-oxide), two among several such paths; these individual configurations are taken together as the TS ensemble that mediates 2MH alkene to 3MH alkene methyl shift isomerization, and the TS free energy for this reaction is given by the free energy of this TS ensemble (Eq. (9); as discussed later in this section for primary isomerization events of linear heptenes). The free energy barriers ($\langle \Delta G^{\ddagger} \rangle$, Eq. (10)) relevant for the formation rates of each isomer thus reflect the free energy of such a TS ensemble, referenced to a bare proton and to the ensemble of equilibrated gaseous heptenes (nC$_7^=$, structures in Scheme 3a). The free energies of a large number (>20) of individual TS structures were calculated for each reaction pathway (e.g., 2MH alkene to 3MH

alkene methyl shift) in order to accurately sample the relevant potential energy surface for these transformations.

The free energy barrier for the conversion of linear heptenes to 2-methylhexenes ($\langle \Delta G^{\ddagger} \rangle$ = 48.0 kJ mol^{-1}) (Scheme 1a) is smaller than for their conversion to 3-methylhexenes ($\langle \Delta G^{\ddagger} \rangle$ = 54.3 kJ mol^{-1}), consistent with selectivities that favor 2MH as the initial isomer formed on Al-MCM-41 at low conversions (Fig. 3). β-Scission reactions of linear heptenes exhibit much larger barriers ($\langle \Delta G^{\ddagger} \rangle$ = 86.0 kJ mol^{-1}), a consequence of the nearly-formed primary carbocation fragment at their TS [67]. The methyl shifts that interconvert 2-methylhexenes and 3-methylhexenes are more facile ($\langle \Delta G^{\ddagger} \rangle$ = 25.5 kJ mol^{-1}) than the formation of either 2- or 3-methylhexenes from linear heptenes. As a result, the two methylhexene skeletal isomers rapidly equilibrate and are treated as a lumped pseudo-species in all kinetic analyses that consider their respective subsequent conversions to other products. Indeed, methylhexenes convert to dimethylpentenes ($\langle \Delta G^{\ddagger} \rangle$ = 44.0 kJ mol^{-1}) and to β-scission products ($\langle \Delta G^{\ddagger} \rangle$ = 78.0 kJ mol^{-1}) with much higher barriers than for their interconversion via methyl shifts ($\langle \Delta G^{\ddagger} \rangle$ = 25.5 kJ mol^{-1}). The interconversion reactions of 24DMP, 23DMP, 22DMP, and 33DMP alkenes also show much lower free energy barriers ($\langle \Delta G^{\ddagger} \rangle$ = 21.9 kJ mol^{-1} for 24DMP to 23DMP alkene methyl shift) than dimethylpentene β-scission ($\langle \Delta G^{\ddagger} \rangle$ = 46.0 kJ mol^{-1}; to form propene and isobutene) or isomerization ($\langle \Delta G^{\ddagger} \rangle$ = 44.0 kJ mol^{-1} to form methylhexenes). Consequently, dimethylpentenes can also be treated as equilibrated chemical pseudo-species that act as the predominant isomer that undergoes β-scission, because their activation free energies are much smaller than for β-scission events of linear heptenes or methylhexenes ($\langle \Delta G^{\ddagger} \rangle$ = 86.0 and 78.0 kJ mol^{-1}, respectively).

The reaction network derived from these theoretical estimates is depicted in Scheme 1b using the saturated analogs of each alkene. Such pathways include the primary routes for the transformation of nC$_7$ to 2MH and 3MH isomers that rapidly interconvert and for their subsequent isomerization to an equilibrated pool of dimethylpentanes that act as the predominant precursors to β-scission products. Primary nC$_7$ reaction events form only 2MH and 3MH isomers. The total isomerization rate thus reflects their combined formation rates, which equal the combined formation rates of all skeletal isomers and β-scission products (j; r_j) because they all form via sequential reactions of the primary 2MH or 3MH alkenes:

$$r_{\text{isom,nC}_7} = \sum_j r_j \tag{16}$$

These rates are expressed here as the number of nC$_7$ molecules appearing as each product.

Fig. 4 shows $r_{\text{isom,nC}_7}$ values (per H$^+$) on MFI-1, BEA-1, SFH-1, and FAU zeolites as a function of the nC$_7$/H$_2$ reactant ratios that determine linear heptene regioisomer concentrations (Section 3.1); the $r_{\text{isom,nC}_7}$ values (per H$^+$) for all other solid acids are included in the SI (S9). Turnover rates at all nC$_7$/H$_2$ ratios are smallest on FAU and increase with decreasing aluminosilicate void size, defined here as the diameter of the largest sphere that can be contained within each framework (d_{LCS}; Table 1). Such differences in reactivity reflect concomitant differences in TS stabilization by van der Waals contacts between hosts and guests, which depend sensitively on their respective sizes. Turnover rates increased linearly with nC$_7$/H$_2$ ratio then reached constant values on all solid
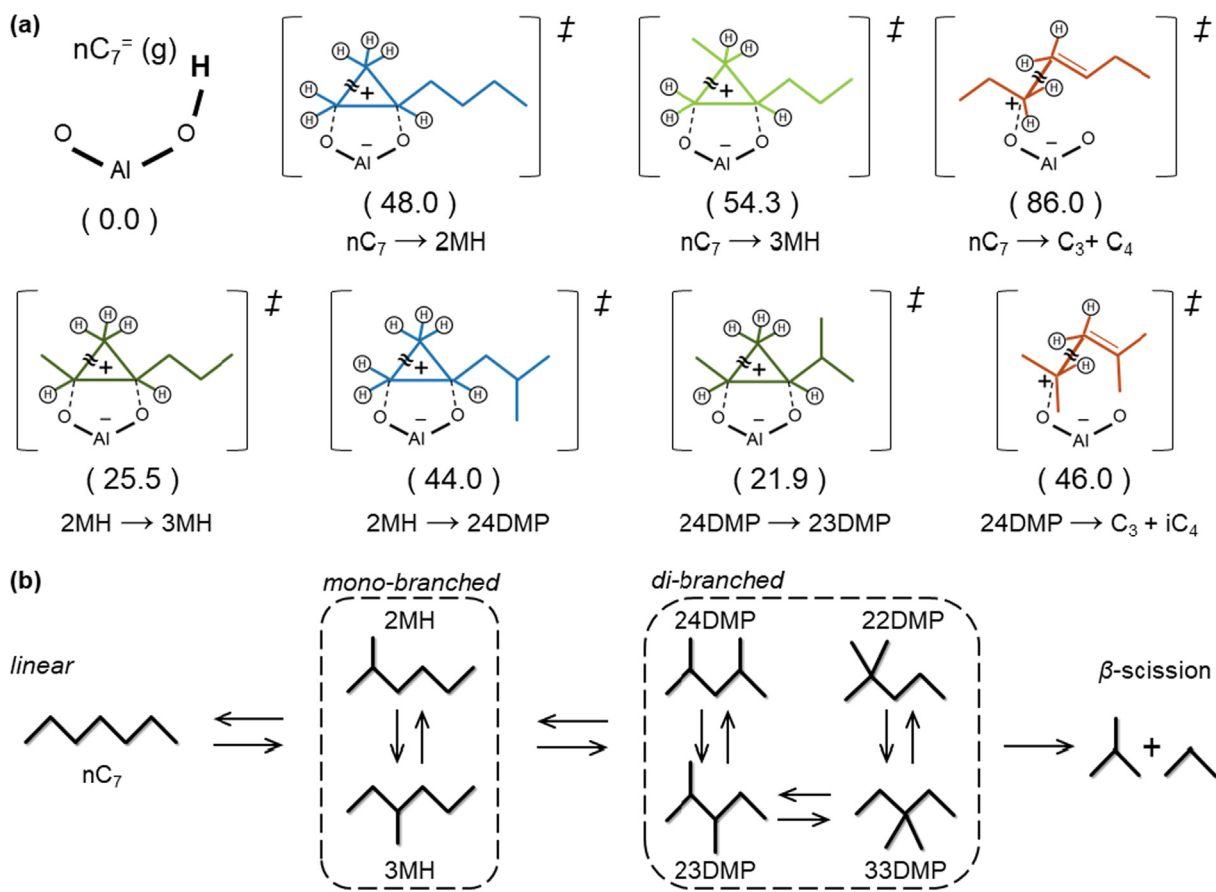
Scheme 1. (a) Schematics of transition states mediating primary and secondary isomerization and β-scission. DFT-derived Gibbs free energies (in kJ mol^{-1}) are indicated in parentheses for transition state ensembles converged at the MFI Al12 at 548 K, standard state (1 bar) (structures included in SI, S6), and calculated with respect to acid sites and equilibrated gas-phase linear heptenes (nC$_7^=$). Lines in transition state structures bisected by a double dash indicate C—C bonds being broken. (b) Isomerization and β-scission reaction network for C$_7$ alkanes on bifunctional physical mixtures of solid Brønsted acids and Pt/SiO$_2$. Dashed boxes around isomers of same degree of branching indicate their rapid interconversion.

acids (Fig. 4; S9, SI), indicating that similar kinetically-relevant elementary steps are involved in the isomerization of *n*-heptenes on these solid acids.

The elementary steps in Scheme 2 lead to a rate equation (Eq. (23); derivation in S8, SI) that accurately describes the measured effects of nC$_7$/H$_2$ reactant ratios on isomerization rates (dashed curves in Fig. 4 and S9, SI). The specific elementary steps in Scheme 2 convert hept-3-oxide to 2-methylhex-1-oxide (Scheme 2, step 3) and illustrate one of many possible primary nC$_7$ isomerization pathways (as discussed below). The Pt function equilibrates *n*-heptane with all linear heptene regioisomers (*trans*-2-heptene shown as an illustrative example; Scheme 2, step 1). Linear heptenes react with protons to form equilibrated mixtures of bound alkoxides with different attachment points at framework O-atoms (Scheme 2, step 2, shown for *trans*-2-heptene and its bound hept-3-oxide). Bound heptoxides then skeletally rearrange to give alkoxides with a different backbone structure in the sole irreversible elementary step (Scheme 2, step 3, shown for 2-methylhex-1-oxide formed from hept-3-oxide). The TS structures that mediate such skeletal isomerization events are essentially full ion pairs (carbocation charge (QUAMBO), δ$^+$ = +0.88; S6, SI); the anion is the conjugate base of the Brønsted acid and the cation is an alkyl-substituted cyclopropyl carbenium ion that undergoes concerted C—C bond formation and cleavage (structures in S6, SI). The product alkoxides desorb as gaseous alkene isomers through β-hydrogen elimination steps that return protons to framework O-atoms (Scheme 2, step 4, shown for 2-methyl-1-
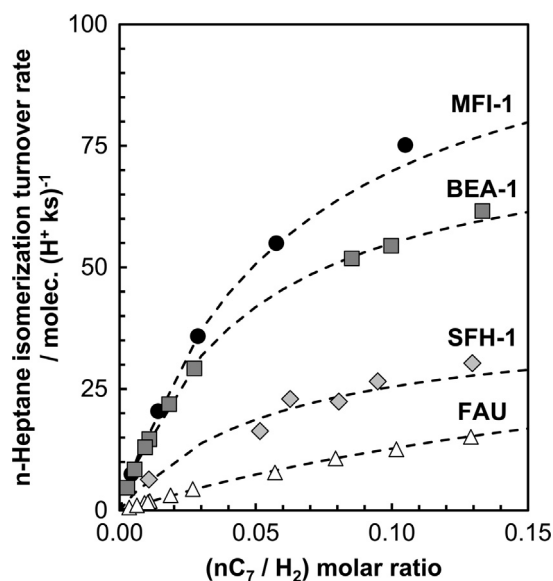

Fig. 4. *n*-Heptane isomerization turnover rates (per H$^+$) as a function of nC$_7$/H$_2$ molar ratio on physical mixtures of Pt/SiO$_2$ with MFI-1 (circles; Pt$_s$/H$^+$ = 9.6), BEA-1 (squares; Pt$_s$/H$^+$ = 12), SFH-1 (diamonds; Pt$_s$/H$^+$ = 11.6), and FAU (triangles; Pt$_s$/H$^+$ = 8.1) (60–100 kPa H$_2$, 548 K). Dashed curves represent regression of rate data to the functional form of Equation (23).

(1) Dehydrogenation

(2) Protonation (adsorption)

(3) Isomerization

(4) Deprotonation (desorption)
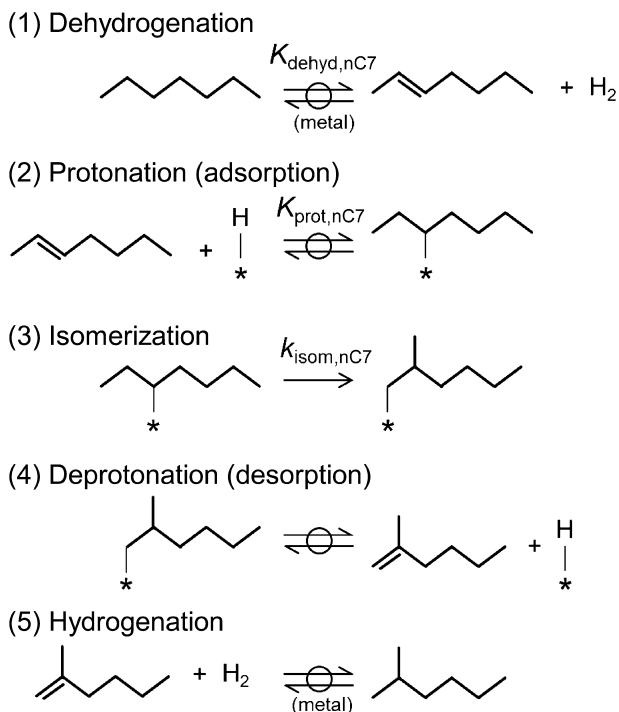
(5) Hydrogenation

Scheme 2. Elementary steps involved in *n*-heptane isomerization on physical mixtures of solid Brønsted acids and Pt/SiO$_2$. Alkane dehydrogenation (step 1) and alkene hydrogenation (step 5) are equilibrated (indicated by the circle overlaying double arrows) on the metal function. Steps 3–5 are shown for products with 2-methylhexane backbone, but analogous steps form 3-methylhexane. "*" in molecular structures denotes points of attachment of protons and alkoxides to aluminosilicate structures. Double-bond regioisomers and surface alkoxides of a given backbone are each treated rigorously as equilibrated lumps, although only 2-heptene, hept-3-oxide, 2-methylhex-1-oxide and 2-methylhex-1-ene are shown here for convenience.

hexene formed from 2-methylhex-1-oxide). These alkene isomers diffuse through acid domains and can readsorb and undergo reactions that form other alkene isomers or smaller chains, until they hydrogenate at the extracrystalline Pt function to form equilibrium amounts of the alkane with the same skeletal backbone (Scheme 2, step 5; 2-methylhexane from 2-methyl-1-hexene).

Scheme 2 shows the elementary steps that form 2-methylhex-1-oxides from hept-3-oxides, one of the rearrangements that contributes to *n*-heptane isomerization events. Analogous sequences can be used to describe the transformations of each heptoxide attachment isomer to specific methylhexoxides. These sets of elementary steps, taken together with the assumptions of quasi-equilibrated dehydrogenation-hydrogenation steps and quasi-equilibrated protonation-deprotonation steps, lead to the rate equation:

$$\frac{r_{\text{isom,nC}_7}}{[\text{H}^+]} = \frac{\sum_a\sum_b\sum_c k_{\text{a,b}}K_{\text{b,c}}K_{\text{c,ref}}K_{\text{dehyd,ref}}(\text{nC}_7/\text{H}_2)}{1 + \sum_b\sum_c K_{\text{b,c}}K_{\text{c,ref}}K_{\text{dehyd,ref}}(\text{nC}_7/\text{H}_2) + \sum_{\text{prod}}K_{\text{prod}}(\text{prod})}$$

$$(17)$$

Here, $k_{\text{a,b}}$ is the rate constant for skeletal isomerization of the "b" heptoxide attachment isomer, mediated via the TS configuration "a"; $K_{\text{b,c}}$ is the equilibrium constant for adsorption of the heptene "c" to form heptoxide "b"; $K_{\text{c,ref}}$ is the equilibrium constant for the formation of gaseous heptene "c" from a chosen reference gaseous heptene regioisomer ("ref"); and $K_{\text{dehyd,ref}}$ is the equilibrium constant for the formation of the reference heptene ("ref") from *n*-heptane. K_{prod} is the equilibrium constant for the adsorption of product alkenes, but their summation ($\sum_{\text{prod}}K_{\text{prod}}(\text{prod})$) contributes negligibly to site coverages at the high reactant/

product ratios prevalent at low nC$_7$ conversions. The assumption of bare protons and bound heptoxides as the most abundant surface intermediates (MASI) then gives the rate equation:

$$\frac{r_{\text{isom,nC}_7}}{[\text{H}^+]} = \frac{\sum_a\sum_b\sum_c k_{\text{a,b}}K_{\text{b,c}}K_{\text{c,ref}}K_{\text{dehyd,ref}}(\text{nC}_7/\text{H}_2)}{1 + \sum_b\sum_c K_{\text{b,c}}K_{\text{c,ref}}K_{\text{dehyd,ref}}(\text{nC}_7/\text{H}_2)}$$

$$(18)$$

which represents the summation of all possible routes that convert *n*-heptene reactants to their primary methylhexene products.

The free energy differences that determine each of the kinetic and thermodynamic constants in Equation (18) are given by:

$$k_{\text{a,b}} = \frac{k_{\text{B}}T}{h}\exp\left(-\frac{G_a^\ddagger - G_b^*}{k_{\text{B}}T}\right)$$

$$(19a)$$

$$K_{\text{b,c}} = \exp\left(-\frac{G_b^* - G_c^= - G^{\text{H}^+}}{k_{\text{B}}T}\right)$$

$$(19b)$$

$$K_{\text{c,ref}} = \exp\left(-\frac{G_c^= - G^{\text{ref}=(\text{g})}}{k_{\text{B}}T}\right)$$

$$(19c)$$

$$K_{\text{dehyd,ref}} = \exp\left(-\frac{G^{\text{ref}=(\text{g})} - G^{\text{nC}_7(\text{g})} - G^{\text{H}_2(\text{g})}}{k_{\text{B}}T}\right)$$

$$(19d)$$

with superscripts ‡, *, and = standing for TS, bound alkoxides, and gaseous alkenes. G^{H^+}, $G^{\text{ref}=(\text{g})}$, $G^{\text{nC}_7(\text{g})}$, and $G^{\text{H}_2(\text{g})}$ denote the free energies of bare protons, the reference heptene regioisomer, gas-phase nC$_7$, and gas-phase H$_2$ (T is the absolute temperature, k_{B} is the Boltzmann constant, h is Planck's constant). Substituting Eq. (19) into Eq. (18), together with the ensemble free energies (denoted by $\langle\ \rangle$) defined by Equation (9), gives, in the case of heptoxides as the sole MASI ($\sum_b\sum_c K_{\text{b,c}}K_{\text{c,ref}}K_{\text{dehyd,ref}}(\text{nC}_7/\text{H}_2) \gg 1$), an expression for the rate constant for the skeletal isomerization step ($k_{\text{isom,nC}_7}$):

$$k_{\text{isom,nC}_7} = \frac{\sum_a\sum_b\sum_c k_{\text{a,b}}K_{\text{b,c}}K_{\text{c,ref}}}{\sum_b\sum_c K_{\text{b,c}}K_{\text{c,ref}}}$$

$$= \frac{k_{\text{B}}T}{h}\frac{\sum_a\exp\left(-\frac{G_a^\ddagger}{k_{\text{B}}T}\right)}{\sum_b\exp\left(-\frac{G_b^*}{k_{\text{B}}T}\right)}$$

$$= \frac{k_{\text{B}}T}{h}\exp\left(-\frac{\langle G^\ddagger\rangle - \langle G^{\text{nC}_7*}\rangle}{k_{\text{B}}T}\right)$$

$$(20)$$

which is the zero-order rate constant. $\langle G^\ddagger\rangle$ is the free energy of the ensemble of TS (Section 2.4) and $\langle G^{\text{nC}_7*}\rangle$ is the free energy of the ensemble of equilibrated heptoxides. A similar treatment when bare protons are the sole MASI ($1 \gg \sum_b\sum_c K_{\text{b,c}}K_{\text{c,ref}}K_{\text{dehyd,ref}}(\text{nC}_7/\text{H}_2)$ in Eq. (18)) and the use of a rigorously referenced equilibrium constant for the dehydrogenation of gaseous species:

$$K_{\text{dehyd,nC}_7} = \sum_c K_{\text{c,ref}}K_{\text{dehyd,ref}}$$

$$(21)$$

combine to give the first-order isomerization rate constant ($k_{\text{isom,nC}_7}K_{\text{prot,nC}_7}$):

$$k_{\text{isom,nC}_7}K_{\text{prot,nC}_7} = \frac{\sum_a\sum_b\sum_c k_{\text{a,b}}K_{\text{b,c}}K_{\text{c,ref}}K_{\text{dehyd,ref}}}{\sum_c K_{\text{c,ref}}K_{\text{dehyd,ref}}}$$

$$= \frac{k_{\text{B}}T}{h}\frac{\sum_a\exp\left(-\frac{G_a^\ddagger - G^{\text{H}^+}}{k_{\text{B}}T}\right)}{\sum_c\exp\left(-\frac{G_c^=}{k_{\text{B}}T}\right)}$$

$$= \frac{k_{\text{B}}T}{h}\exp\left(-\frac{\langle G^\ddagger\rangle - \langle G^{\text{nC}_7=(\text{g})}\rangle - G^{\text{H}^+}}{k_{\text{B}}T}\right)$$

$$(22)$$

where $\left\langle G^{\mathrm{nC_7^=(g)}} \right\rangle$ is the free energy of the ensemble of equilibrated gaseous linear heptenes (Eq. (9)). These kinetic treatments consider equilibrated linear heptenes and equilibrated heptoxides each as ensembles, with their ensemble free energies given by $\left\langle G^{\mathrm{nC_7^=(g)}} \right\rangle$ and $\left\langle G^{\mathrm{nC_7^*}} \right\rangle$, respectively (in Eqs. (20) and (22)). These equilibrated ensembles are denoted here by the superscript "=" for alkenes and by the superscript "*" for alkoxides (e.g., $\mathrm{nC_7^=}$ and $\mathrm{nC_7^*}$; structures of equilibrated species in $\mathrm{nC_7^=}$ and $\mathrm{nC_7^*}$ ensembles are shown in Scheme 3a).

The kinetic and thermodynamic parameters defined in Eqs. (20)-(22) can be used to obtain the rate expression in Equation (18) as:

$$\frac{r_{\mathrm{isom,nC_7}}}{[\mathrm{H^+}]} = \frac{k_{\mathrm{isom,nC_7}} K_{\mathrm{prot,nC_7}} K_{\mathrm{dehyd,nC_7}} (\mathrm{nC_7/H_2})}{1 + K_{\mathrm{prot,nC_7}} K_{\mathrm{dehyd,nC_7}} (\mathrm{nC_7/H_2})} \tag{23}$$

where $K_{\mathrm{prot,nC_7}}$ is the equilibrium constant for alkoxide formation, $K_{\mathrm{dehyd,nC_7}}$ (Eq. (21)) is the equilibrium constant for $\mathrm{nC_7}$ dehydrogenation to an equilibrated mixture of all linear heptene regioisomers, and $k_{\mathrm{isom,nC_7}}$ (Eq. (20)) is the rate constant for the isomerization of

(a)

$\mathrm{nC_7^=}$

$\mathrm{nC_7^*}$

(b)
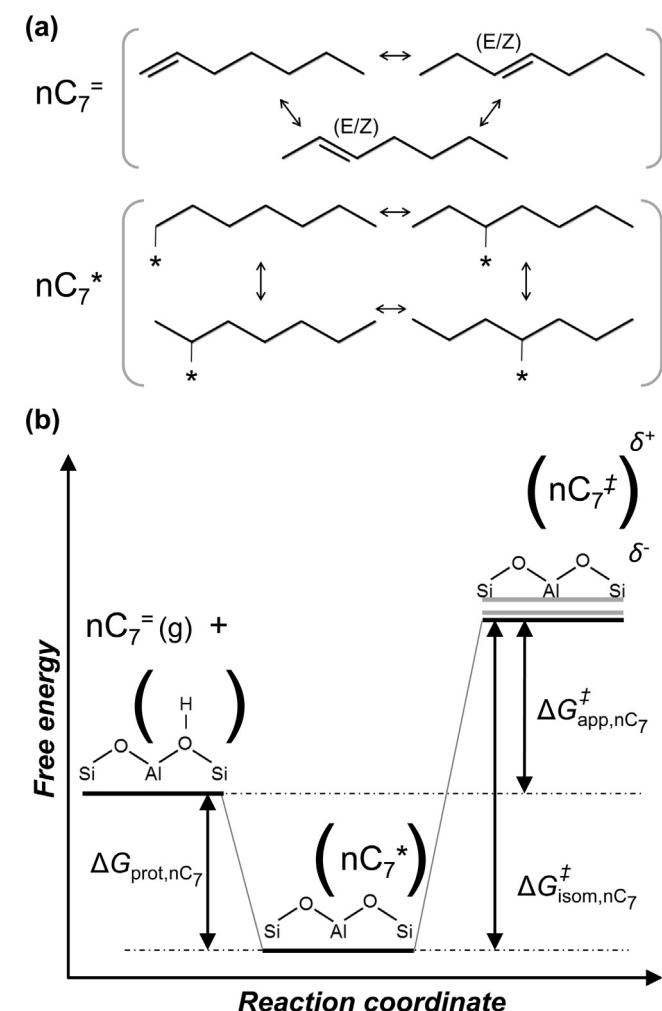
Scheme 3. (a) Structures of double-bond regioisomers within equilibrated linear heptenes ($\mathrm{nC_7^=}$) and alkoxides with different attachment points to aluminosilicate structures (denoted by "*") within equilibrated heptoxides ($\mathrm{nC_7^*}$). (b) Reaction coordinate diagram indicate the free energies that account for rate constants (per $\mathrm{H^+}$) for n-heptane isomerization. Horizontal gray lines at the transition state represent the free energies of individual transition state configurations, while the horizontal black line represents the free energy of the transition state ensemble.

$\mathrm{nC_7^*}$ to the lumped equilibrated $\mathrm{MH^*}$ products; the first-order rate constant is given by $k_{\mathrm{isom,nC_7}} K_{\mathrm{prot,nC_7}}$ (Eq. (22)). These $k_{\mathrm{isom,nC_7}} K_{\mathrm{prot,nC_7}}$ and $k_{\mathrm{isom,nC_7}}$ values were determined by regressing all rate data to the functional form of Equation (23) and using available thermodynamic data for $K_{\mathrm{dehyd,nC_7}}$ (19.8 Pa at 548 K [30,31]). Table 2 shows $k_{\mathrm{isom,nC_7}} K_{\mathrm{prot,nC_7}}$ and $k_{\mathrm{isom,nC_7}}$ values for each aluminosilicate solid acid. The $k_{\mathrm{isom,nC_7}}$ values cannot be accurately measured because they require high heptene pressures for kinetically-detectable alkoxide coverages favoring oligomerization events that form less reactive residues and cause detectable deactivation. Measured $k_{\mathrm{isom,nC_7}} K_{\mathrm{prot,nC_7}}$ values differ by about 10^3-fold among these aluminosilicates at conditions that preclude any effects of intracrystalline $\mathrm{nC_7^=}$ concentration gradients on rates (Section 3.1).

Scheme 3b shows a reaction coordinate diagram consistent with the elementary steps in Scheme 2 and with Equation (23). The free energies that determine the zero-order ($\left\langle \Delta G^{\ddagger}_{\mathrm{isom,nC_7}} \right\rangle$) and first-order ($\left\langle \Delta G^{\ddagger}_{\mathrm{app,nC_7}} \right\rangle$) rate constants are given by:

$$\begin{aligned} k_{\mathrm{isom,nC_7}} &= \frac{k_B T}{h} \exp\left(\frac{-\left\langle \Delta G^{\ddagger}_{\mathrm{isom,nC_7}} \right\rangle}{k_B T} \right) \\ &= \frac{k_B T}{h} \exp\left(-\frac{\left\langle G^{\mathrm{nC_7^\ddagger}} \right\rangle - \left\langle G^{\mathrm{nC_7^*}} \right\rangle}{k_B T} \right) \end{aligned} \tag{24a}$$

$$\begin{aligned} k_{\mathrm{isom,nC_7}} K_{\mathrm{prot,nC_7}} &= \frac{k_B T}{h} \exp\left(\frac{-\left\langle \Delta G^{\ddagger}_{\mathrm{app,nC_7}} \right\rangle}{k_B T} \right) \\ &= \frac{k_B T}{h} \exp\left(-\frac{\left\langle G^{\mathrm{nC_7^\ddagger}} \right\rangle - \left\langle G^{\mathrm{nC_7^=(g)}} \right\rangle - G^{\mathrm{H^+}}}{k_B T} \right) \end{aligned} \tag{24b}$$

$\left\langle G^{\mathrm{nC_7^\ddagger}} \right\rangle$ and $\left\langle G^{\mathrm{nC_7^*}} \right\rangle$ values, but not $\left\langle G^{\mathrm{nC_7^=(g)}} \right\rangle$, which is a property of gaseous species, are both influenced by confinement and thus by the geometry of zeolitic voids.

Transition state energies depend sensitively on van der Waals contacts and on the "fit" between the aluminosilicate hosts and the organic guest species [9,10]. As a result, $k_{\mathrm{isom,nC_7}} K_{\mathrm{prot,nC_7}}$ values depend on void size (Fig. 5), typically derived from spherical constructs, such as the diameter of the largest sphere that can be inscribed within a given void structure (d_{LCS}, Table 1). The size of the carbocation moieties at $\mathrm{nC_7}$ isomerization transition states can also be described by similar metrics, such as the diameter of the sphere of equivalent volume (d_{eq}) or surface area ($d_{\mathrm{eq,SA}}$) (as indicated by the shaded region (0.636–0.698 nm) in Fig. 5), where these carbocation volumes and surface areas are obtained from Connolly surfaces [55] (Section 2.4). These descriptors give similar sizes for the carbocations that mediate $\mathrm{2MH^=}$ and $\mathrm{3MH^=}$ formation from $\mathrm{nC_7^=}$; all individual TS carbocations within a given TS ensemble that converts specific heptoxides to specific methylhexoxides are similar in size by these metrics (<0.5% difference in either d_{eq} or $d_{\mathrm{eq,SA}}$; Table 3). The first-order rate constants for $\mathrm{nC_7}$ isomerization increase about ten-fold as the void size decreases from that of Al-MCM-41 mesopores ($d_{\mathrm{LCS}} = 2.5$ nm) to that of FAU supercages ($d_{\mathrm{LCS}} = 1.1$ nm), consistent with more effective van der Waals contacts as confining voids approach the size of the relevant TS carbocation (0.636–0.698 nm). These trends continue for smaller voids (SFH, BEA, and MFI, respectively), as such fits become tighter and TS carbocations increasingly stabilized by van der Waals contacts.

As voids become even smaller, van der Waals contacts require significant distortions of the organic guest and the inorganic host; the consequent enthalpic penalties lead to destabilization of TS structures (relative to adsorbed precursors) and to lower reactivity on the acid sites that reside within these smaller voids [9,10]. $\mathrm{nC_7}$
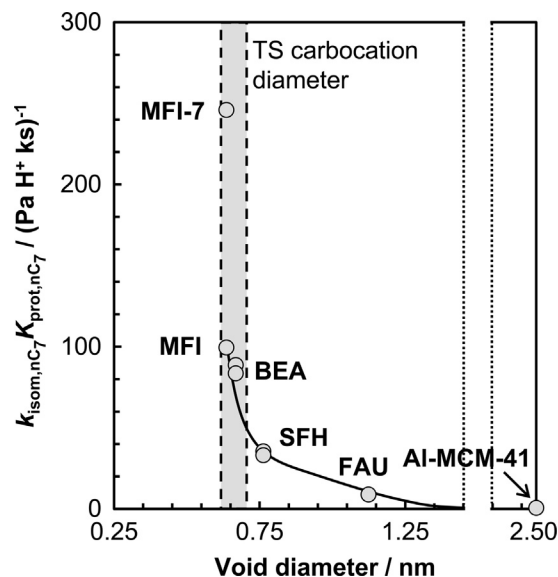
Fig. 5. n-Heptane first-order isomerization rate constant ($k_{isom,nC_7}K_{prot,nC_7}$, per H$^+$; 548 K) for aluminosilicates with different void sizes (diameter of the largest contained sphere [27]). Shaded area between vertical dashed lines is the range of diameters for the nC$_7$ isomerization transition-state carbocation. The rate constants denoted "MFI" represents averaged values for MFI-1–5. Solid curve represents trends.

isomerization is a monomolecular rearrangement involving reactants and TS carbocations of similar size. As a result, tight confinement within voids becomes synonymous with larger diffusional barriers, which can lead to intracrystalline concentration gradients and to rates that reflect only indirectly the stability of relevant isomerization TS structures. Consequently, confinement effects on intrinsic reactivity cannot be examined for such systems without accounting for these intracrystalline concentration gradients of alkene reactants.

MFI samples with a broad range of proton density (0.35–2.8 H$^+$/unit cell (u.c.); Table 4) gave similar first-order rate constants (MFI-1–5; 95.5–123 (Pa H$^+$ ks)$^{-1}$, Table 2; mean value plotted in Fig. 5). These MFI samples vary in ρ_{H^+} and R^2/D_{22DMB} values, but their simplified Thiele moduli (Ξ^2 in Eq. (15)) are small ($\Xi^2 < 6$ s cm^{-3}; Fig. 2), thus precluding any consequences of nC$_7^=$ concentration gradients on measured turnover rates (Section 3.1). The strong effects of confinement on first-order rate constants ($k_{isom,nC_7}K_{prot,nC_7}$, Fig. 5) and the similar values measured on these MFI samples indicate that protons reside within similar void environments, specifically at the intersections of straight and sinusoidal channels (d_{LCS} = 0.636 nm). Previous studies have inferred from mechanistic interpretations of kinetic data the nearly exclusive presence of protons at intersections in MFI samples with this range of proton densities (0.35–2.8 H$^+$/u.c., Table 4) [47].

The MFI sample with the highest proton density (MFI-7; 4.2 H$^+$/u.c., Table 4), shows a two-fold higher first-order rate constant (258 (Pa H$^+$ ks)$^{-1}$; Fig. 5) than the other MFI samples, even though

Table 4
Proton density and extraframework Al contents for MFI samples.

Acid	H$^+$/u.c.	Al$_{ex}$/u.c.[*]
MFI-1	0.67	1.4
MFI-2	2.0	1.1
MFI-3	1.9	0.24
MFI-4	0.35	0.22
MFI-5	2.9	0.0
MFI-6	1.7	0.93
MFI-7	4.2	1.3

[*] Estimated as the Al without an associated proton.

its Ξ^2 value (19.9 s cm^{-3}) would indicate some kinetic consequences of incipient intracrystalline nC$_7^=$ concentration gradients. These gradients would have led to smaller rate constants than on the other MFI samples, which lack such gradients. The higher reactivity of protons within MFI-7 must therefore reflect more stable TS structures, possibly because of their location within the more restrictive void environment provided by channels. Extraframework Al species at MFI intersections may also lead to smaller local environments, as shown for Al$_2$O$_3$ detrital species within FAU [68]. These non-framework Al species are not more prevalent, however, in MFI-7 (1.3 Al/u.c., Table 4) than in the other MFI samples (0.22–1.4 Al/u.c., Table 4). The number of such Al atoms per intersection (0.06–0.35 Al/intersection) in these samples is also much smaller than that required for reactivity enhancements on FAU ($\sim$4) [68]. As a result, it seems unlikely that local void narrowing by detrital Al species could account for the higher reactivity observed on MFI-7. We conclude that Al sites incipiently occupy the minority T-sites present within channels, leading to tighter confinement of isomerization TS carbocations, as also concluded for methanol dehydration on these same MFI samples [47].

These conclusions are consistent with energetic estimates of van der Waals stabilization of TS carbocations (reported below) but may seem at first glance implausible because MFI channel diameters (0.47 nm) are smaller than the size of spherical proxies for nC$_7$ isomerization TS carbocations (0.636–0.698 nm). Such constructs, however, inherently neglect the precise shapes of hosts and guests, which are essential in establishing van der Waals contacts. Table 3 includes a nonsphericity index (v) for these TS carbocations, defined as the ratio of the longest chord through the carbocation to the diameter of the equivalent sphere, d_{eq} (Section 2.4). These v values are significantly larger than unity (1.51–1.52) for nC$_7$ isomerization TS carbocations, because they resemble ellipsoids or cylinders. Heuristic descriptions of size based on spherical constructs must be replaced by estimates of van der Waals interaction energies, which rigorously account for size and shape. These more precise descriptors of TS stability indeed show that isomerization TS carbocations are more effectively stabilized within MFI channels than at MFI channel intersections (Fig. 6). These van der Waals interaction energies and their consequences for the reactivity of confined protons are examined next.

3.3. Effects of transition state confinement on n-heptane isomerization turnover rates and selectivities

van der Waals interaction energies (E_{vdw}) are determined here using Lennard-Jones potentials and statistical sampling methods that place transition state carbocations at each crystallographically unique, accessible T-site within each zeolite framework. nC$_7$ isomerization TS were optimized at the MFI Al12 site using functionals that account for the dispersive interactions between the framework and the carbocation (Section 2.4); the carbocation from the TS with the smallest DFT-derived free energy was selected as the representative TS carbocation among all TS structures that convert nC$_7^=$ to specific MH*, because its free energy contributes most significantly to the free energy of the TS ensemble. This TS carbocation was used as the structure that samples each T-site location in each zeolite, without additional optimization of the energy or geometry of either the host or the guest in response to the different local environment at each location, to calculate interaction energies ($\langle E_{vdw}\rangle_T$, Eq. (12); more negative values indicating greater stability) at each T-site within FAU, SFH, BEA, and MFI (described in Section 2.4.1) [10].

The $\langle E_{vdw}\rangle$ values for each framework structure were obtained from $\langle E_{vdw}\rangle_T$ values (using Eq. (13), by assuming random Al placement at all T-sites within each framework for SFH and BEA (FAU

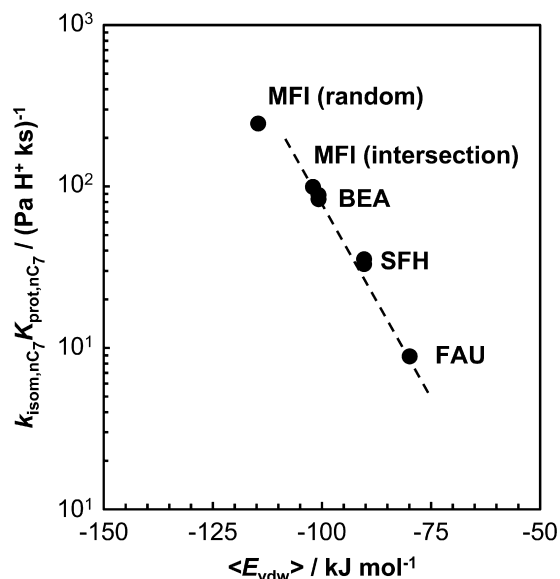**Fig. 6.** n-Heptane first-order isomerization rate constant ($k_{\text{isom,nC}_7} K_{\text{prot,nC}_7}$; per H$^+$; 548 K) as a function of van der Waals interaction energies, $\langle E_{\text{vdw}} \rangle$, for nC$_7$ isomerization transition state carbocations within aluminosilicates. The "MFI (intersection)" rate constant represents the average value for MFI-1–5; its $\langle E_{\text{vdw}} \rangle$ value is for carbocations placed at MFI intersections only. The rate constant for MFI-7 is denoted as "MFI (random)" and its $\langle E_{\text{vdw}} \rangle$ includes placement of carbocations at all locations within MFI. The dashed line is the regressed exponential fit of the measured $k_{\text{isom,nC}_7} K_{\text{prot,nC}_7}$ values (Eq. (25b)) and omits MFI (random) because it exhibits concentration gradients of heptenes.

has only one T-site; thus, $\langle E_{\text{vdw}} \rangle = \langle E_{\text{vdw}} \rangle_T$). The $\langle E_{\text{vdw}} \rangle$ values for MFI were evaluated for two different Al placement schemes: (i) random Al siting (denoted as "random" and "(r)") and (ii) Al siting only at intersections ("intersection" and "(i)"). Such alternate schemes become relevant for MFI because of the very different confining environments at intersections and channels, which contrast the similar local environments at all T-sites within each given framework for the other zeolites. $\langle E_{\text{vdw}} \rangle$ values for TS carbocations placed only at intersections (-105 kJ mol^{-1}) are less negative than for random Al siting (-119 kJ mol^{-1}), which includes TS carbocations located within channels; these differences are consistent with the less effective van der Waals contacts at intersections than within channels. Such findings, which we address in detail below, provide compelling evidence for the incomplete and inaccurate nature of size descriptors that neglect shape in assessments of the consequences of van der Waals interactions for reactivity.

The $k_{\text{isom,nC}_7} K_{\text{prot,nC}_7}$ kinetic parameters increase exponentially as $\langle E_{\text{vdw}} \rangle$ becomes more negative and TS carbocations more stable through confinement effects (Fig. 6). These trends reflect the contributions of $\langle E_{\text{vdw}} \rangle$ to activation free energies ($\langle \Delta G_{\text{app,nC}_7}^{\ddagger} \rangle$, Eq. (24b); Scheme 3b), which can be expressed in terms of their enthalpy ($\langle \Delta H_{\text{app,nC}_7}^{\ddagger} \rangle$) and entropy ($\langle \Delta S_{\text{app,nC}_7}^{\ddagger} \rangle$) components:

$$\frac{\partial \left(\ln \left(k_{\text{isom,nC}_7} K_{\text{prot,nC}_7} \right) \right)}{\partial \left(\langle E_{\text{vdw}} \rangle \right)} = -\frac{1}{k_B T} \frac{\partial \left(\langle \Delta H_{\text{app,nC}_7}^{\ddagger} \rangle - T \langle \Delta S_{\text{app,nC}_7}^{\ddagger} \rangle \right)}{\partial \left(\langle E_{\text{vdw}} \rangle \right)} \tag{25a}$$

At moderate temperatures, such as those of isomerization catalysis, enthalpic effects more than compensate for entropy losses upon confinement ($\langle \Delta H_{\text{app,nC}_7}^{\ddagger} \rangle \gg T \langle \Delta S_{\text{app,nC}_7}^{\ddagger} \rangle$, Eq. (25a)). Activation enthalpies are obtained here from electronic energies ($\langle E_{\text{app}} \rangle$) after temperature corrections using translational, rotational, and vibrational energies. These corrections are insensitive to any small

changes in the degrees of freedom of TS carbocations caused by their slightly different structures at each T-site in each zeolite, thus allowing the use of $\langle E_{\text{app}} \rangle$ instead of $\langle \Delta H_{\text{app,nC}_7}^{\ddagger} \rangle$ in Equation (25a):

$$\frac{\partial \left(\ln \left(k_{\text{isom,nC}_7} K_{\text{prot,nC}_7} \right) \right)}{\partial \left(\langle E_{\text{vdw}} \rangle \right)} = -\frac{1}{k_B T} \frac{\partial \left(\langle E_{\text{app}} \rangle \right)}{\partial \left(\langle E_{\text{vdw}} \rangle \right)} \tag{25b}$$

The dashed line in Fig. 6 represents the regression of measured rate constants to the functional form of Equation (25b); this regression does not include the $k_{\text{isom,nC}_7} K_{\text{prot,nC}_7}$ value for MFI-7 (denoted as MFI "random"), because intracrystalline nC$_7^=$ concentration gradients lead to a rate constant smaller than predicted by $\langle E_{\text{vdw}} \rangle$ trends in Fig. 6.

These trends in first-order rate constants with $\langle E_{\text{vdw}} \rangle$ (Fig. 6) are examined next using a Born-Haber thermochemical cycle (Scheme 4) [69] in order to assess how catalyst and molecular properties influence activation barriers. This cycle exploits the state function nature of thermodynamic properties in constructing a sequence of hypothetical steps that form the TS structure; these steps are arbitrary but rendered convenient because they decouple the effects of catalyst and molecular properties on activation barriers.

The thermochemical cycle in Scheme 4 includes steps that: (i) deprotonate the acid and remove the proton to non-interacting distances (deprotonation energy, DPE), (ii) form the ensemble of gaseous carbocation analogs for the nC$_7^=$ to MH* ensemble of transition states by protonating a gaseous nC$_7^=$ molecule at each possible location (proton affinity, $\langle E_{\text{prot}} \rangle$), and (iii) place the gaseous cations at the distance from the conjugate anion corresponding to that in the ion-pair TS structure (interaction energy, $\langle E_{\text{app}} \rangle$). The last step can be further dissected into: (iiia) an electrostatic component ($\langle E_{\text{es}} \rangle$), given by the energy recovered through Coulombic interactions as the gaseous carbocation approaches the conjugate anion; (iiib) a van der Waals component ($\langle E_{\text{vdw}} \rangle$), given by dispersive interactions; and (iiic) a structural component ($\langle E_{\text{str}} \rangle$) that accounts for the energy required to distort both the
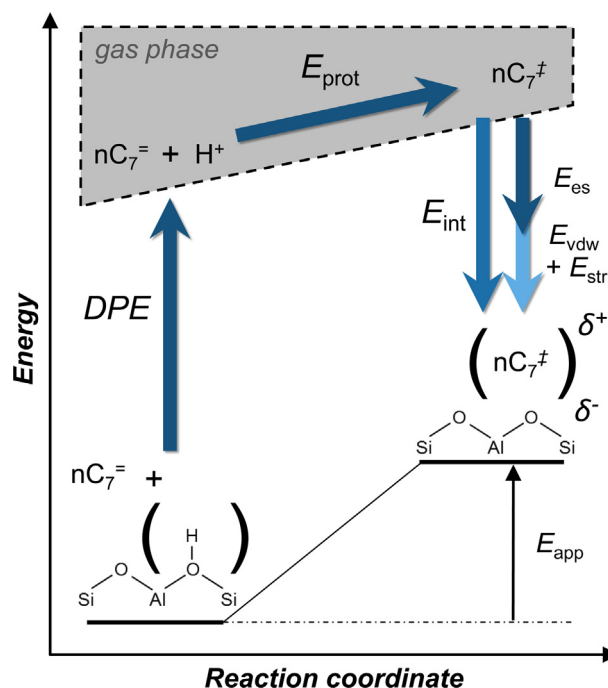
Scheme 4. Thermochemical cycle representing activation barriers for acid-catalyzed alkene isomerization in terms of hypothetical constituent steps, with the respective energies reflected in first-order rate constants (E_{app}).

framework and the carbocation in order to form the most stable host–guest complex:

$$\langle E_{app} \rangle = DPE + \langle E_{prot} \rangle + \langle E_{int} \rangle$$
$$= DPE + \langle E_{prot} \rangle + \langle E_{es} \rangle + \langle E_{vdw} \rangle + \langle E_{str} \rangle \quad (26)$$

Measured $k_{isom,nC_7} K_{prot,nC_7}$ values increase exponentially as $\langle E_{vdw} \rangle$ becomes more negative (Fig. 6). The expected change in $\langle E_{app} \rangle$ values with changes in $\langle E_{vdw} \rangle$ induced by confinement is given by the derivative of Equation (26) with respect to $\langle E_{vdw} \rangle$:

$$\frac{\partial (\langle E_{app} \rangle)}{\partial (\langle E_{vdw} \rangle)} = \frac{\partial (DPE + \langle E_{prot} \rangle + \langle E_{es} \rangle + \langle E_{vdw} \rangle + \langle E_{str} \rangle)}{\partial (\langle E_{vdw} \rangle)}$$
$$= 1 + \frac{\partial (\langle E_{str} \rangle)}{\partial (\langle E_{vdw} \rangle)} \quad (27)$$

DPE values are insensitive to van der Waals interactions because protons and conjugate anions do not benefit detectably from changes in void geometry [70], while the $\langle E_{prot} \rangle$ term is a property of gaseous $nC_7^=$ molecules; as a result, neither *DPE* nor $\langle E_{prot} \rangle$ values sense the geometry of the confining void.

The $\langle E_{es} \rangle$ term in Equation (26) accounts for electrostatic interactions between conjugate anions and the gaseous proxies of TS carbocations, which depend on the charge distribution within each component of the ion-pair TS. Such charge distributions are similar for all zeolite frameworks, because acid sites are of similar strength and conjugate anions show similar stability at all locations within each framework. The distance (l_{cs}, Table 3) between the zeolite T-site, which is the conjugate anion center-of-charge (QUAMBO), and the TS carbocation center-of-charge depends very weakly on the relative size of the TS carbocation to the zeolite void, even when TS structures were relaxed in response to the local void environment, for a series of homologous transition state carbocations (Section 2.4.1; S7, SI). These distances (l_{cs}, in Table 3) were therefore kept constant in the assessment of $\langle E_{vdw} \rangle$ for TS carbocations at each T-site in each zeolite. Consequently, $\langle E_{es} \rangle$ values are unaffected by the geometric details of each local environment.

The linear trend shown in Fig. 6 indicates that $\frac{\partial (\langle E_{app} \rangle)}{\partial (\langle E_{vdw} \rangle)}$ (= 0.48) remains the same for all void structures, in spite of their 100-fold differences in reactivity (Fig. 6). This slope is smaller than unity, indicating that $\langle E_{vdw} \rangle$ is only used partially to stabilize the TS; isomerization TS structures become more stable for tighter host–guest fits but only by a fraction of the concomitant changes in $\langle E_{vdw} \rangle$. This fraction ($\frac{\partial (\langle E_{app} \rangle)}{\partial (\langle E_{vdw} \rangle)}$) reflects the energy penalties imposed by structural distortions in hosts and guests ($\langle E_{str} \rangle$ in Scheme 4; Eq. (27)) required to form the van der Waals contacts that lead to minimum overall TS free energies. Larger void structures contract in order to form more effective contacts with the organic guests, while smaller voids expand to avoid repulsion as the TS carbocations and voids become similar in size, as shown previously from quantitative metrics of these framework distortion [11]. These framework distortions cannot be measured here because the protocols used here to evaluate $\langle E_{vdw} \rangle$ do not geometrically relax the zeolite framework, but their energetic consequences ($\langle E_{str} \rangle$) can be assessed by comparing how these $\langle E_{vdw} \rangle$ values affect measured rate constants, which reflect minimum overall free energies for TS structures in which both hosts and guests are fully relaxed (Eq. (27)). These energy penalties are given by a constant fraction of $\langle E_{vdw} \rangle$ as shown in Fig. 6 by a constant slope ($\frac{\partial (\langle E_{str} \rangle)}{\partial (\langle E_{vdw} \rangle)} = -0.52$; Eq. (27)), indicating that the energy costs associated with atomic displacements become more consequential for frameworks that provide tighter confinement and thus more negative values of $\langle E_{vdw} \rangle$. Such trends reflect the higher atomic densities in the frameworks that form these more effective contacts with organic guests (MFI: 18.4 T atoms nm^{-3}; FAU: 13.3 T atoms nm^{-3} [27]), which

require displacement of a larger number of framework atoms. These compensating factors lead to similar effects of $\langle E_{vdw} \rangle$ on experimental $\langle E_{app} \rangle$ values for all zeolites and thus to the observed constant value of $\frac{\partial (\langle E_{app} \rangle)}{\partial (\langle E_{vdw} \rangle)}$ (Eq. (27); Fig. 6).

These confinement effects, shown here for the formation of primary products $MH^=$ (equilibrated $2MH^=$ and $3MH^=$; Section 3.2) from $nC_7^=$, also affect the rates of formation of secondary products, with consequences for selectivity that depend on any differences in van der Waals contacts among the TS carbocations that mediate secondary isomerization and β-scission reactions. The effects are assessed here through $\langle E_{vdw} \rangle$ estimates for representative TS carbocations. The values for each zeolite are shown in Fig. 7, together with $\langle E_{vdw} \rangle$ values for the TS that forms $2MH^=$ and $3MH^=$ from $nC_7^=$ in primary isomerization events.

The β-scission carbocation chosen is that for the $24DMP^=$ β-scission TS, which gives DFT-derived free energies much smaller than that for $MH^=$ β-scission (Scheme 1). Secondary isomerization events are examined using the $24DMP^=$ isomerization to $23DMP^=$ TS carbocation at the TS with the smallest DFT-derived free energy, because this specific $24DMP^*$ to $23DMP^*$ TS contributes most significantly to the free energy of the ensemble of all $24DMP^=$-to-$23DMP^=$ isomerization TS; this TS ensemble is chosen to represent secondary isomerization because TS carbocations are shaped most differently (nonsphericity index, $v = 1.45$; Table 3), among all secondary isomerization TS ensembles, from $nC_7^=$ isomerization TS carbocations ($v = 1.51$; Table 3). Consequently, $\langle E_{vdw} \rangle$ values assessed for this $24DMP^=$ isomerization TS carbocation would amplify any differences in TS stabilization for secondary isomerization in each zeolite void, compared to primary $nC_7^=$ isomerization.

The TS carbocations for $24DMP^=$ isomerization and β-scission cannot be placed within MFI channels during statistical sampling, in the absence of framework relaxation. These effects arise because atoms in the TS carbocation and in the zeolite framework approach too closely when neither structure is relaxed, thus causing spurious repulsive interactions detected by Lennard-Jones potentials that are very sensitive to atom–atom distances. These repulsive
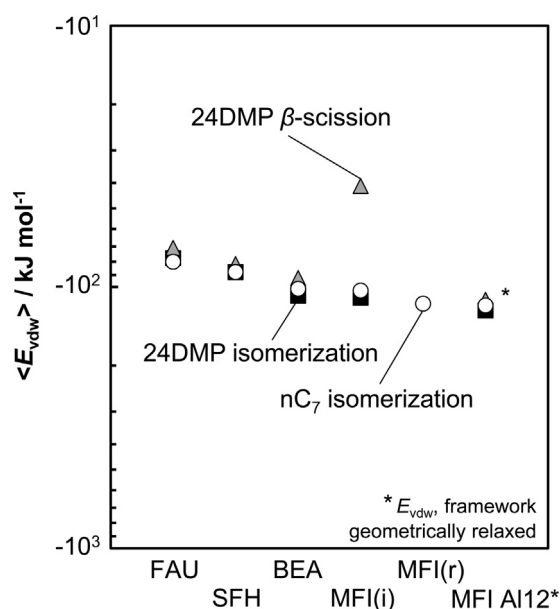

Fig. 7. The van der Waals interaction energy ($\langle E_{vdw} \rangle$) for *n*-heptane isomerization (circles), 2,4-dimethylpentane isomerization (squares), and 2,4-dimethylpentane β-scission (triangles) transition state carbocations in FAU, SFH, BEA, and MFI(i) (carbocations at the intersection only) and for *n*-heptane isomerization (circles) in MFI(r) (carbocations at all locations in MFI). E_{vdw} values for MFI Al12 are evaluated for DFT-converged transition states at the MFI Al12, where framework atoms have been geometrically relaxed.

interactions also lead to artificially more positive $\langle E_{vdw}\rangle$ values for 24DMP β-scission even in the larger MFI channel intersections (-41 kJ mol^{-1} for 24DMP$^=$ β-scission compared to -110 kJ mol^{-1} for 24DMP$^=$ isomerization in MFI intersections; Fig. 7). van der Waals interaction energies (E_{vdw}) were instead calculated for DFT-optimized TS structures with fully relaxed organic guests and inorganic hosts; these TS were converged at the MFI Al12 at channel intersections and thus reflect that specific local confining environment.

E_{vdw} values are similar for the nC$_7^=$ and 24DMP$^=$ isomerization and 24DMP$^=$ β-scission TS carbocations (-112 to -123 kJ mol^{-1}; Fig. 7) and more negative than $\langle E_{vdw}\rangle$ values in unrelaxed frameworks by 14 and 13 kJ mol^{-1} for nC$_7^=$ and 24DMP$^=$ isomerization TS, respectively, because the framework structure has distorted to minimize overall TS free energies (E_{str}, Eq. (26)). In contrast, 24DMP$^=$ β-scission E_{vdw} is more negative than its $\langle E_{vdw}\rangle$ counterpart (by 71 kJ mol^{-1}; Fig. 7) because of the aforementioned computational artifacts that arise from the absence of geometric relaxation.

These spurious interactions prevent the placement of either 24DMP$^=$ TS carbocation within the smaller channels of MFI. 24DMP$^=$ TS carbocations are more spherical than nC$_7^=$ isomerization TS carbocations (v indices in Table 3), although spherical constructs describe them as similar in size ($d_{eq} = 0.636 - 0.649$ nm; Table 3); nC$_7^=$ isomerization TS carbocations can be placed within MFI channels without framework geometric relaxation because of its more highly ellipsoidal shape. TS structures were not fully optimized using DFT methods at MFI channel positions; comparisons of E_{vdw} for these TS carbocations at such locations are therefore not reported. The high β-scission selectivities on MFI-7 ($\sim$0.70, Section 3.4), which has protons incipiently located within MFI channels, suggest that these spurious interactions cannot be taken as a reflection of transition state destabilization. We surmise that the full electronic and geometric optimization of 24DMP$^=$ TS at MFI channels would yield values of E_{vdw} that are similar to each other and to that for nC$_7^=$ TS.

In each large void structure (FAU, SFH, BEA) and in MFI intersections after framework relaxation, $\langle E_{vdw}\rangle$ values (Fig. 7) are similar for primary and secondary reactions TS carbocations for each given framework. A void of a given size and shape forms similar van der Waals contacts with each of the TS carbocations that mediate primary and secondary isomerization and secondary β-scission reactions. As a result, confinement effects cannot influence the relative rates of the steps mediated by such TS structures, leading to intrinsic selectivities that cannot sense the shape and size of the confining voids.

Measured product selectivities, however, differ among zeolite frameworks (Fig. 10b); in general, secondary β-scission products are favored for frameworks that exhibit higher reactivity and more negative $\langle E_{vdw}\rangle$ values. These structures favor higher β-scission selectivities because of the combined effects of smaller voids, which provide more effective van der Waals contacts but also restrict the diffusional egress of primary alkene products, thus enhancing secondary isomerization and β-scission events. Such diffusion-enhanced secondary reactions, instead of the preferential stabilization of specific transition states by confinement or by acid sites of different strengths, are responsible for the observed selectivity differences among zeolites with different void structures, as shown through quantitative descriptions in the next section.

3.4. Consequences of diffusion-enhanced secondary isomerization and β-scission for selectivity

The effects of diffusional constraints on selectivity are examined here using reaction–diffusion treatments based on mole balances for reactant and product alkenes within acid domains [71,72]. These treatments consider 2MH and 3MH as the only primary products of nC$_7$ reactants, with all other products formed via secondary reactions (Section 3.2). Selectivities on zeolitic acids may be generally affected by confinement of the TS carbocations that mediate primary and secondary reactions, but in this case, the TS structures are stabilized to similar extents by any void of a given size and shape (Section 3.3). Secondary transformations can occur as primary alkene isomers diffuse within acid domains; they are favored on zeolite structures with more effective confining interactions, which increase turnover rates on acid sites and also restrict molecular diffusion, especially for the more highly branched (and more reactive) isomers.

Selectivities during nC$_7$ isomerization on zeolites are nearly insensitive to bed residence times (1.64–8.75 (H$^+$ s) molec.$^{-1}$) (selectivities: 0.84–0.81 for MH, 0.14–0.16 for β-scission; MFI-3, Fig. 8a) and to nC$_7$/H$_2$ reactant ratio (0.005–0.15) (selectivities: 0.86–0.82 for MH, 0.13–0.14 for β-scission; MFI-3, Fig. 8b). These selectivities are essentially unaffected by titrating protons with an irreversibly-bound base (DTBP) on large-pore zeolites (FAU, BEA; BEA-1, Fig. 8c), through which such large bases can diffuse. Such titrations occur sequentially along the catalyst bed, thus causing a monotonic decrease in the effective bed length. Changes in residence time of nearly a factor of ten, caused by varying either inlet molar flow rates or effective bed length by titration, do not lead to detectable effects on selectivity. These data show that secondary reactions do not occur in the timescale of their passage through the catalyst bed, after alkene products egress from acid domains and hydrogenate at the extracrystalline Pt function.

Fig. 8d shows β-scission selectivities as a function of bed residence time on MFI-2, MFI-3, and MFI-4. These samples give similar first-order rate constants (Section 3.3) and similar characteristic diffusion times ($R^2/D_{22DMB} = 1.09$–1.24×10^4 s, Table 1) but differ in their proton density ($\rho_{H^+} = 0.35$–2.0 H$^+$/u.c., Table 4). These β-scission selectivities reflect solely the prevalence of secondary reactions of alkene products; they increased (from 0.04 to 0.32) with increasing ρ_{H^+} (0.35 to 2.0 H$^+$/u.c.; Fig. 8d). These strong effects of ρ_{H^+} on β-scission selectivity, taken together with selectivity values that are insensitive to bed residence time, indicate that selectivities are determined by reactions that occur within a given acid domain, before product alkenes are hydrogenated at the extracrystalline Pt function. The contributions from these reactions depend, in turn, on zeolite intracrystalline residence times through effects of proton density that increase the probability of readsorption and secondary reactions during one passage through acid domains.

Intracrystalline residence times ($\tau_{zeo,i}$ for molecule i) are given by:

$$\tau_{zeo,i} = \frac{\rho_{H^+}R^2}{D_i} \tag{28}$$

where D_i is the diffusivity of molecule i. The product of intracrystalline residence times and the first-order rate constants for reactions that consume molecule i (k_i) is:

$$k_i\tau_{zeo,i} = \frac{k_i\rho_{H^+}R^2}{D_i} = \phi_i^2 \tag{29}$$

where ϕ_i is the Thiele modulus for these consumption reactions of molecule i. Eq. (29) shows that $\tau_{zeo,i}$ values are proportional to ϕ_i^2 for each specific zeolite framework, which also exhibits a value of k_i that is a unique reflection of its confining voids. These ϕ_i values reflect the severity of intracrystalline gradients of molecule i. Larger ϕ_i values are indicative of more severe concentration gradients, as a result of faster reactions, slower diffusion, larger crystallite sizes, or a higher volumetric density of acid sites, with the last accounting for the observed increase in β-scission selectivity as ρ_{H^+} increases within acid domains (Fig. 8d).
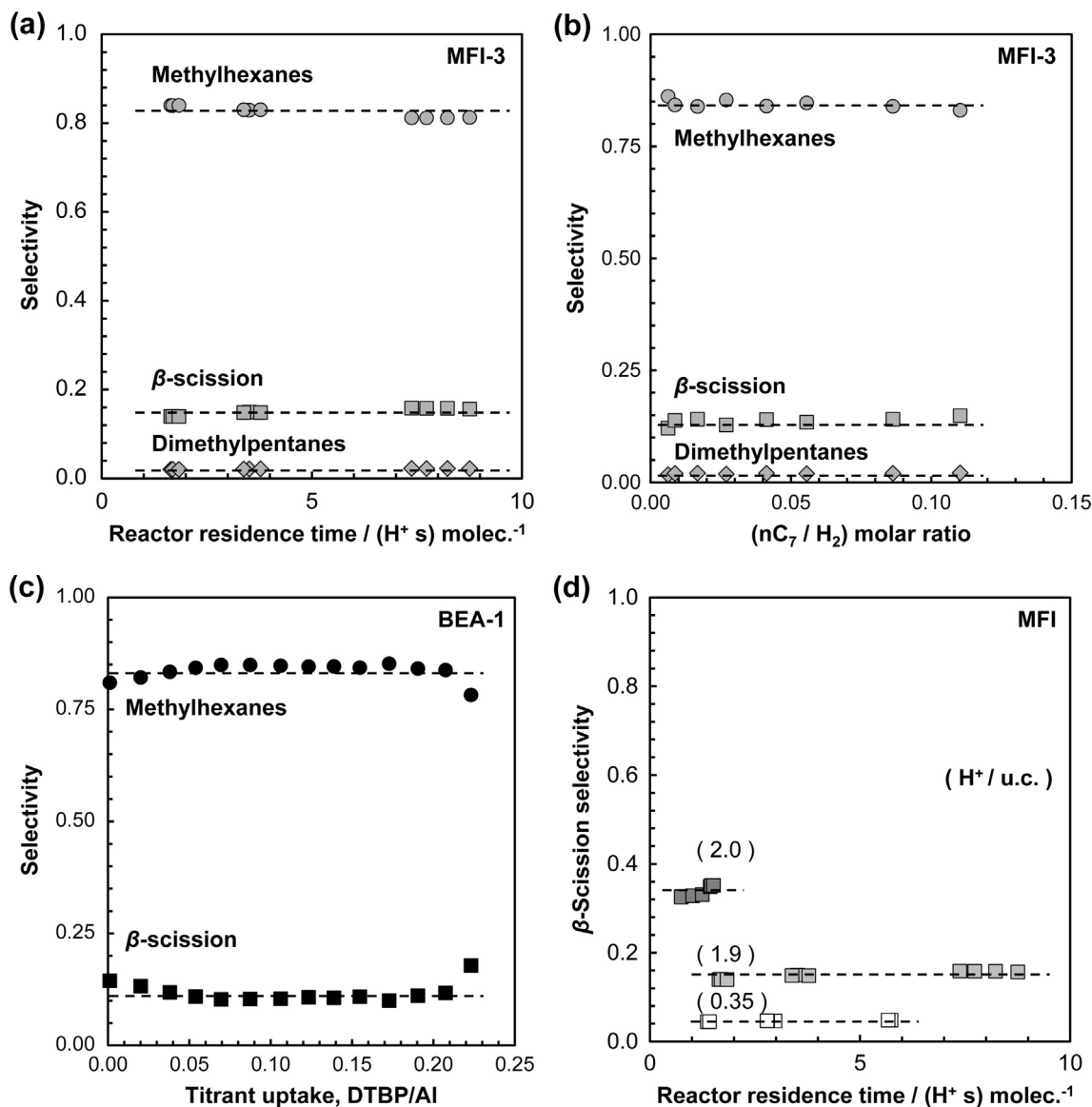
Fig. 8. (a) Measured product selectivities (methylhexanes, circles; β-scission, squares; dimethylpentanes, diamonds) as a function of reactor residence time (0.01–0.02 nC$_7$/H$_2$ molar ratio) and (b) as a function of nC$_7$/H$_2$ molar ratio during nC$_7$ isomerization on a physical mixture of Pt/SiO$_2$ and MFI-3; (c) measured product selectivities (methylhexanes, circles; β-scission, squares) during titration with DTBP on a physical mixture of Pt/SiO$_2$ and BEA-1 (0.11–0.48 Pa DTBP, 0.01–0.02 nC$_7$/H$_2$ molar ratio); and (d) measured β-scission selectivity during *n*-heptane isomerization as a function of reactor residence time (0.01–0.02 nC$_7$/H$_2$ molar ratio) on physical mixtures of Pt/SiO$_2$ with MFI samples with similar $R^2/D_{22\text{DMB}}$ values but different acid site densities (H$^+$/u.c.: 0.35, white; 1.9, light gray; 2.0, dark gray). (Differential nC$_7$ conversion (<10%), 60–100 kPa H$_2$, 548 K) The dashed horizontal lines depict average selectivities.

These effects of intracrystalline residence times are also evident from the selectivities observed with monotonic changes in ρ_{H^+} caused by the gradual desorption of preadsorbed NH$_3$ titrants during nC$_7$ isomerization reactions (method in Section 2.2.1). nC$_7$ isomerization rates on FAU and BEA-2 (shown as illustrative examples) increase systematically with time as NH$_3$ titrants desorb (Fig. 9a); these rates are proportional to the number of protons that become available as NH$_3$ titrants are removed.

Fig. 9b shows MH, DMP, and β-scission selectivities as protons become available during NH$_3$ desorption on FAU and BEA-2. On both samples, DMP and β-scission products are not detected at the low ρ_{H^+} values prevalent during the initial stages of NH$_3$ desorption, consistent with their exclusive formation via diffusion-enhanced secondary reactions (Section 3.2) that occur infrequently when intracrystalline domains contain only a few protons. DMP and β-scission selectivities increase and MH selectivities decrease

as NH$_3$ desorbs and ρ_{H^+} concurrently increases. Such higher proton densities favor sequential transformations of MH$^=$ to DMP$^=$ and of DMP$^=$ to β-scission products (propene and isobutene); they also lead to larger MH$^=$ and DMP$^=$ Thiele moduli (Eqs. (30) and (31)) and to a shift in products from those formed in single sojourns at acid sites to those ultimately prescribed by the thermodynamic stability of gaseous alkenes.

The selectivity to products formed in a single acid site sojourn (Eq. (4)) can be determined from these data (Fig. 9b) by extrapolation to the initial stages of NH$_3$ desorption ($\tau_{\text{zeo,i}} \rightarrow 0$). Such primary selectivities are indeed zero for DMP and β-scission products on FAU and BEA-2 (Fig. 9b). Confinement effects on TS stability for secondary reactions therefore require an assessment of the effects of intracrystalline residence time on DMP and β-scission selectivities through the use of coupled reaction–diffusion models that describe selectivities in terms of the relevant Thiele moduli.
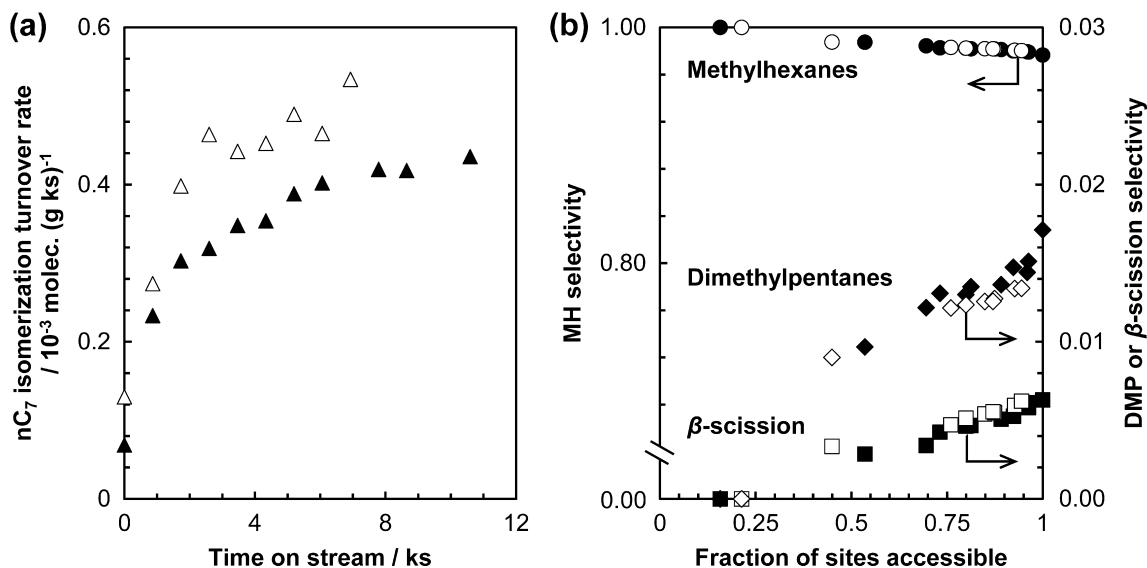
Fig. 9. (a) Measured *n*-heptane isomerization turnover rate (per g) as a function of time-on-stream during NH_3 desorption and (b) product selectivities (methylhexanes, circles, left; *β*-scission, squares, right; dimethylpentanes, diamonds, right) as a function of fraction of sites rendered accessible by the desorption of NH_3) during *n*-heptane isomerization on a physical mixture of Pt/SiO_2 and FAU (black) or BEA-2 (white) (0.015 nC_7/H_2 molar ratio, 100 kPa H_2, 548 K).

These dimensionless Thiele parameters for $MH^=$ to $DMP^=$ isomerization ($\phi_{MH^=}$) are given by:

$$\phi_{MH^=}^2 = \frac{k_{isom,MH}K_{prot,MH}\rho_{H^+}R^2}{D_{MH^=}} \tag{30}$$

and for $DMP^=$ *β*-scission ($\phi_{DMP^=}$) by:

$$\phi_{DMP^=}^2 = \frac{k_{\beta,DMP}K_{prot,DMP}\rho_{H^+}R^2}{D_{DMP^=}} \tag{31}$$

where $D_{MH^=}$ and $D_{DMP^=}$ are $MH^=$ and $DMP^=$ diffusivities, respectively. The $k_{isom,MH}K_{prot,MH}$ term represents the first-order rate constant for $MH^=$ isomerization to $DMP^=$ and $k_{\beta,DMP}K_{prot,DMP}$ is the first-order rate constant for $DMP^=$ *β*-scission. The ratio of these two Thiele moduli is:

$$\kappa^2 = \frac{\phi_{DMP^=}^2}{\phi_{MH^=}^2} = \frac{k_{\beta,DMP}K_{prot,DMP}}{D_{DMP^=}}\frac{D_{MH^=}}{k_{isom,MH}K_{prot,MH}} \tag{32}$$

It reflects the ratio of $DMP^=$ and $MH^=$ diffusivities and of the reaction rate constants (per H^+) for their respective consumption reactions; the magnitude of κ is independent of the size or proton density of the acid domains, and it attains a unique value for each given framework.

The diffusive and reactive properties represented by the parameters in Eqs. (30) and (31) cannot be directly obtained from nC_7 isomerization reaction rate and selectivity data. We define an effective Thiele modulus for $nC_7^=$ ($\Phi_{nC_7^=}$) that includes independently measurable parameters: rate constants ($k_{isom,nC_7}K_{prot,nC_7}$; from rate data and Eq. (23); Section 3.2; Table 2), diffusion timescales (R^2/D_{22DMB}; transient uptakes at 448 K; Section 2.3; Table 1) from transient sorption measurements (Section 2.3), and proton densities (ρ_{H^+}) (Section 2.2.1):

$$\Phi_{nC_7^=}^2 = \frac{k_{isom,nC_7}K_{prot,nC_7}\rho_{H^+}R^2}{D_{22DMB}} \tag{33}$$

Both $k_{isom,nC_7}K_{prot,nC_7}$ and R^2/D_{22DMB} are unique properties of each given sample, and specifically of its framework structure and crystallite size, respectively. The ρ_{H^+} term is varied systematically for each sample by the gradual desorption of NH_3 titrants (Fig. 9b for FAU and BEA-2; Fig. 10 for all zeolites). This effective Thiele

modulus ($\Phi_{nC_7^=}$, Eq. (33)) is proportional to that derived from a rigorous analysis of the reaction-transport mole balance equations ($\phi_{nC_7^=}$; derivation in S10, SI):

$$\phi_{nC_7^=}^2 = \frac{k_{isom,nC_7}K_{prot,nC_7}\rho_{H^+}R^2}{D_{nC_7^=}} \tag{34}$$

The proportionality between the Thiele moduli in Eqs. (33) and (34) is given by the ratio of diffusivities for $nC_7^=$ (at 548 K) and for 22DMB (at 448 K) ($D_{nC_7^=}/D_{22DMB}$).

The $MH^=$ Thiele modulus (Eq. (30) can be divided by $\Phi_{nC_7^=}$(Eq. (33) to define a parameter, λ:

$$\lambda^2 = \frac{\Phi_{nC_7^=}^2}{\phi_{MH^=}^2} = \frac{D_{MH^=}}{k_{isom,MH}K_{prot,MH}}\frac{k_{isom,nC_7}K_{prot,nC_7}}{D_{22DMB}} \tag{35}$$

As in the case of κ (Eq. (32), λ is independent of proton density or acid domain size and represents the intrinsic reactive and diffusive properties of each framework type. Consequently, κ and λ values provide insights into the diffusional enhancements of secondary reactions by elucidating the consequences of void structure for the relative ratios of diffusivities and rate constants in Eqs. (32) and (35).

Product selectivities are measured as a function of $\Phi_{nC_7^=}$, varied through desorption of bound NH_3, and are regressed to the functional form of Eqs. (36)–(38) below. These expressions were obtained from the pathways in Scheme 1b, together with the elementary steps in Scheme 2 (with bare protons as MASI), and reaction-transport formalisms for quasi-spherical acid domains (S10, SI). MH selectivities are given by:

$$S_{MH} = \frac{3\lambda^2}{\Phi_{nC_7^=}^2}\left(\frac{\Phi_{nC_7^=}}{\lambda}\coth\left(\frac{\Phi_{nC_7^=}}{\lambda}\right) - 1\right) \tag{36}$$

and DMP selectivities are given by:

$$S_{DMP} = \frac{3\lambda^2}{\kappa^2\Phi_{nC_7^=}^2}\left(\frac{1}{1-\kappa^2}\left(\kappa\frac{\Phi_{nC_7^=}}{\lambda}\coth\left(\kappa\frac{\Phi_{nC_7^=}}{\lambda}\right)\right.\right.$$
$$\left.\left. - \kappa^2\frac{\Phi_{nC_7^=}}{\lambda}\coth\left(\frac{\Phi_{nC_7^=}}{\lambda}\right)\right) - 1\right) \tag{37}$$

Here, λ (Eq. (35)) and κ (Eq. (32)) represent parameters that can differ among frameworks but that do not depend on proton density
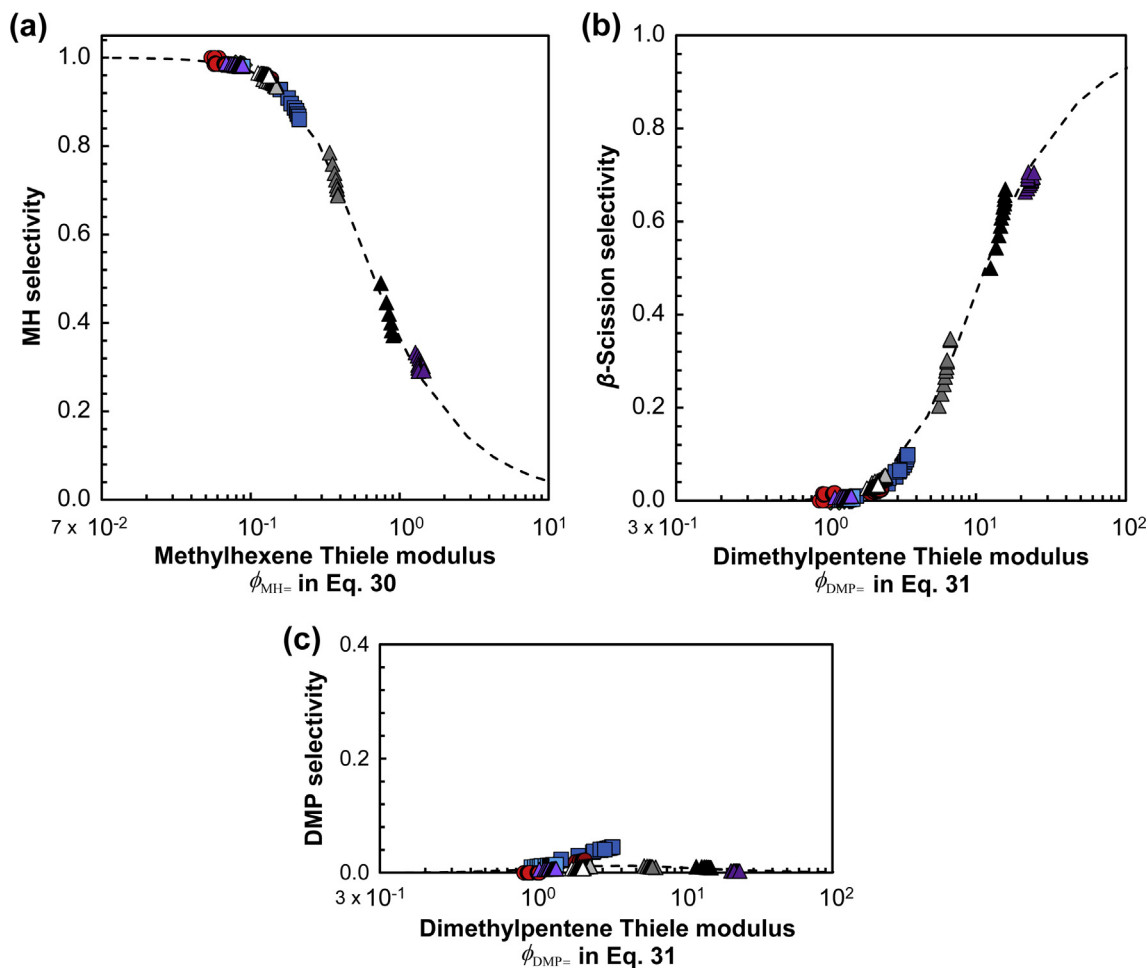
Fig. 10. Measured selectivities to (a) methylhexane products as a function of the methylhexane Thiele modulus, $\phi_{\text{MH=}}$(Eq. (30), varied by desorption of NH_3) and (b) β-scission and (c) dimethylpentane products as a function of the dimethylpentene Thiele modulus, $\phi_{\text{DMP=}}$(Eq. (31), varied by desorption of NH_3) during nC_7 isomerization on physical mixtures of Pt/SiO_2 and FAU (green diamonds), SFH (red circles), BEA (blue squares), MFI (white, gray, black, and purple triangles) (548 K). Dashed curves represent regression of data to the functional form of Eqs. (36) and (37) in (a), (b), and (c), respectively.

and acid domain size. The fractional β-scission selectivities are obtained from Eqs. (36) and (37) by difference:

$$S_\beta = 1 - S_{\text{MH}} - S_{\text{DMP}} \tag{38}$$

Product selectivities were measured on all zeolites over a broad range of ρ_{H^+} during NH_3 desorption and at conditions leading to the first-order rate dependences (0.01–0.02 nC_7/H_2 molar ratios). Fig. 10a shows that MH selectivities as $\phi_{\text{MH=}}$ (Eq. (30)) increase with increasing ρ_{H^+} values on all acids. MH selectivities are near unity for small $\phi_{\text{MH=}}$ (<1) but decrease monotonically as $\phi_{\text{MH=}}$ increases. These MH selectivities were regressed to the functional form of Equation (36) using the same value of λ (Eq. (35)) for all samples with a given zeolite framework in order to relate $\Phi_{nC_7^=}$ values (Eq. (33)) to $\phi_{\text{MH=}}$ values.

Eqs. (36–38) rigorously describe selectivities on acid domains that do not exhibit kinetically consequential intracrystalline gradients of linear heptene reactants. The corresponding expressions for selectivities in systems exhibiting concentration gradients of both reactant and product alkenes (MFI-6, MFI-7) are given in the SI (S10), along with the details of their mathematical derivations. These expressions require an additional parameter, χ, which is given by:

$$\chi^2 = \frac{D_{\text{22DMB}}}{D_{nC_7^=}} \frac{k_{\text{isom},nC_7} K_{\text{prot},nC_7}}{\left(k_{\text{isom},nC_7} K_{\text{prot},nC_7}\right)_{\text{obs}}} \tag{39}$$

The χ values reflect the ratio of diffusivities for 22DMB (at 448 K) and for $nC_7^=$ (at 548 K) ($D_{\text{22DMB}}/D_{nC_7^=}$) and the ratio of the kinetic to the measured first-order rate constants $\frac{k_{\text{isom},nC_7} K_{\text{prot},nC_7}}{\left(k_{\text{isom},nC_7} K_{\text{prot},nC_7}\right)_{\text{obs}}}$; the diffusivity ratio is much less than unity, while the rate constant ratio is only slightly greater than one. The same λ and κ values were used to relate $\Phi_{nC_7^=}$ values (Eq. (33)) to $\phi_{\text{MH=}}$ and $\phi_{\text{DMP=}}$ on all MFI samples (selectivities on MFI-6 and MFI-7 regressed to expressions in S10, SI; selectivities on MFI-1 – MFI-5 regressed to Eqs. (36–38), because λ and κ are intrinsic to a given zeolite framework and their values do not depend on the severity of the intracrystalline reactant concentration gradients. The regressed values of χ for MFI-6 and MFI-7 (3.5×10^{-4} and 3.0×10^{-4}; Table 5) lead to expressions for MH, DMP, and β-scission selectivities that have the same functional form as those in Eqs. (36–38), which neglect reactant concentration gradients (S10, SI), at least across the measured range of $\Phi_{nC_7^=}$ values; product selectivities for MFI-6 and MFI-7 are thus included in Fig. 10, where the curves represent the regression of data to the functional forms of Eqs. (36–38).

The λ values reflect the ratios of rate constants ($k_{\text{isom},nC_7} K_{\text{prot},nC_7}/k_{\text{isom},MH} K_{\text{prot},MH}$ in Eq. (35)) and diffusivities ($D_{\text{MH=}}/D_{\text{22DMB}}$ in Eq. (35)). These λ values are all of order 10^2 (Table 5), predominantly because $D_{\text{MH=}}$ at 548 K is larger than D_{22DMB} at 448 K. Indeed, methylpentane diffusivities, which are similar to those for methylhexenes [73], are $\sim 10^5$ larger at 548 K

than D_{22DMB} at 448 K on MFI [12,59]. These λ values increase as the void size decreases monotonically from that of FAU to that of MFI, because of concomitant changes in $k_{isom,nC_7}K_{prot,nC_7}/k_{isom,MH}K_{prot,MH}$ or $D_{MH^=}/D_{22DMB}$ ratios among these zeolites. The $k_{isom,nC_7}K_{prot,nC_7}/k_{isom,MH}K_{prot,MH}$ ratios in Equation (35) are expected to depend weakly on the void structure; confinement leads to similar van der Waals contacts with primary and secondary isomerization TS carbocations (Section 3.3). Consequently, the observed increase in λ values with decreasing void size is likely to reflect $D_{MH^=}/D_{22DMB}$ ratios that are larger on smaller voids. The highly branched nature of 22DMB molecules leads to a larger molecular size than MH$^=$ (critical diameter: 0.62 and 0.50 nm, respectively [34]), and the ratio of molecular size to framework aperture size sensitively determines diffusivities [23,34]. As a result, 22DMB diffusivities should be influenced by a decrease in void size more strongly than are MH$^=$ diffusivities. Such effects, as molecular sizes approach those of framework apertures, are the likely cause of the larger λ values for MFI than for FAU (MFI: 746, FAU: 352; Table 5).

Fig. 10b shows β-scission selectivities on all acids as a function of their DMP Thiele moduli ($\phi_{DMP^=}$, Eq. (31)). These β-scission selectivities are zero at small $\phi_{DMP^=}$ values and asymptotically approach unity as $\phi_{DMP^=}$ increases. These selectivities are accurately described by Equation (38) (S10, SI for MFI-6 and MFI-7) with the same κ value (Eq. (32); $\kappa = 7.13$) for all acids. This value of κ reflects the ratio of rate constants ($k_{\beta,DMP}K_{prot,DMP}/k_{isom,MH}K_{prot,MH}$ in Eq. (32)) and diffusivities ($D_{MH^=}/D_{DMP^=}$ in Eq. (32)) for MH$^=$ and DMP$^=$. The similar κ value for all zeolites indicates that neither of these ratios vary from framework to framework, in the absence of fortuitous cancellation or compensating effects; the diffusivity ratio in κ ($D_{MH^=}/D_{DMP^=}$) is greater than unity and unlikely to change with zeolite framework, because even the diffusivity ratios in λ parameters ($D_{MH^=}/D_{22DMB}$ in Eq. (36)), which are expected to be more sensitive to the zeolite framework, only varied by a factor of five from FAU to MFI. Rate constant ratios ($k_{\beta,DMP}K_{prot,DMP}/k_{isom,MH}K_{prot,MH}$) have similar values among frameworks that vary in their first-order rate constants for nC$_7$ isomerization by more than 10^2, indicating that each given zeolite void stabilizes TS carbocations mediating primary and secondary reactions to the same extent. Such findings are consistent with $\langle E_{vdw} \rangle$ estimates for the TS carbocations that mediate 24DMP$^=$ isomerization and β-scission in each zeolite (Fig. 7; Section 3.3).

DMP selectivities are shown as a function of $\phi_{DMP^=}$ in Fig. 10c. These selectivities are near zero for small $\phi_{DMP^=}$ but increase to a maximum value of 0.05 and then decrease for larger $\phi_{DMP^=}$ values. Such trends show that DMP forms only through secondary reactions and subsequently reacts via β-scission as DMP$^=$ gradients become more severe at large $\phi_{DMP^=}$ values. The maximum DMP selectivities achieved (~0.05) reflect the high reactivity and low diffusivities of these branched alkenes relative to their less branched MH analogs.

These reaction-transport models show that MH, DMP, and β-scission selectivities differ among aluminosilicates as a conse-quence of diffusional constraints that enhance contributions from secondary reactions. These effects reflect the higher turnover rates and increasing diffusional barriers as sizes of inorganic voids approach those of the reacting molecules and their transition states and the slower diffusion and higher reactivity of branched alkene isomers. These effects have been previously attributed, inaccurately and without direct evidence, to different effects of confinement on the transition states that mediate the formation of different isomers and of β-scission products and, in some cases, to stronger acid sites in MFI and other medium-pore zeolites than in large-pore zeolites or mesoporous aluminosilicates. In fact, these effects of framework structure on selectivities merely reflect Thiele moduli that determine intracrystalline concentration gradients of product alkenes, instead of any preferential stabilization of specific transition states or any differences in acid strength among aluminosilicates.

4. Conclusions

The effects of confinement on reactivity and selectivity and the effects of diffusional constraints on selectivity are mechanistically assessed here using n-heptane isomerization and β-scission reactions on physical mixtures of Pt/SiO$_2$ with mesoporous and microporous aluminosilicates (Al-MCM-41, FAU, SFH, BEA, and MFI); these materials contain protons of similar acid strength that reside within different confining environments. The use of physical mixtures defines the acid domain, the contiguous region of acid sites separating the metal function, as the aluminosilicate crystallite; this, in turn, permits the assessment of their diffusion timescales, which are proportional to (and a surrogate for) crystallite sizes for a given zeolite framework, by transient uptake measurements of probe sorbate 2,2-dimethylbutane. Physical mixtures of sufficient intimacy equilibrate reactant n-heptane dehydrogenation (to linear heptenes and H$_2$) at the extracrystalline metal function and preclude sub-equilibrium concentrations of reactant alkenes within acid domains. n-Heptane isomerization turnover rates are normalized by the number of accessible protons, allowing rigorous comparison among acids of different confining ability and with free energies from density functional theory calculations.

First-order nC$_7$ isomerization rate constants reflect the free energy difference between isomerization transition states (to form 2MH$^=$ and 3MH$^=$) and gas-phase nC$_7^=$ and bare protons. These first-order rate constants increase with improved "fit" between the organic moiety at the transition state and the inorganic framework, which arise as sizes of voids approach those of confined TS carbocations. These confining interactions are defined rigorously by van der Waals interaction energies (E_{vdw}, calculated using Lennard-Jones potential force fields and statistical sampling methods) that account for sizes and shapes of hosts and guests. E_{vdw} values are similar for the transition state carbocations that mediate primary and secondary isomerization and secondary β-scission reactions of n-heptane in each zeolite, demonstrating that a given void similarly stabilizes all transition states in n-heptane isomerization and β-scission reactions.

Measured selectivities to secondary products, however, differ among mesoporous and microporous aluminosilicates. Only on Al-MCM-41 do selectivities depend on bed residence times, a consequence of the weak confining interactions by and facile molecular diffusion within the mesopores of this acid. Selectivities on zeolites are, in contrast, nearly independent of bed residence times, even for dimethylpentane and β-scission products that are measured at non-zero selectivities in spite of their formation in exclusively secondary reactions. Selectivities to β-scission products are highest for acids with the highest rate constants for nC$_7$ isomerization; among acids of a given framework, β-scission selectivities

Table 5
Values of the fitting parameters, λ (Eq. (35)) and χ (Eq. (39)).

Acid	λ^*
FAU	352 (±13)
SFH	440 (±27)
BEA	675 (±38)
MFI	746 (±7.4)
	$\chi \times 10^{4*}$
MFI-6	3.5 (±0.11)
MFI-7	3.0 (±0.35)

* Unitless.

increase with crystallite sizes and proton densities. Such trends together indicate that for zeolites, product alkene intracrystalline residence times, not bed residence times, determine measured product selectivities. The small pores of zeolites not only stabilize transition states through van der Waals interactions but also impede molecular diffusion, resulting in the occurrence of secondary transformations of primary alkene products as they egress from the acid domain, before they hydrogenate at extracrystalline metal sites.

Reaction-transport formalisms accounting for the diffusional enhancements of these secondary reactions were taken together with selectivities measured during the desorption of weakly bound NH_3 molecules. Such desorption systematically increases the intracrystalline residence times and Thiele moduli of alkene intermediates by increasing the accessible proton density within each acid domain. Reaction-diffusion treatments reveal that measured product selectivities to secondary products are fully described by Thiele moduli for alkene intermediates; product selectivities that vary among zeolite frameworks thus cannot be taken as an indication of preferential stabilization of transition states or of differences in acid strength among zeolites, but rather only as an indication of the specific diffusional constraints imposed by a given solid acid.

5. Notes

The authors declare the following competing financial interest(s):

(1) The funding for this research came from Chevron Energy Technology Co. and
(2) Stacey I. Zones is an employee of this company, more generally, also a stockholder of Chevron Corp.

Appendix A. Supplementary material

Supplementary data associated with this article can be found, in the online version, at https://doi.org/10.1016/j.jcat.2018.03.033.

References

[1] J.W. Ward, Design and preparation of hydrocracking catalysts, Stud. Surf. Sci. Catal. (1983) 587–618, https://doi.org/10.1016/S0167-2991(09)60052-5.
[2] S.J. Miller, New molecular sieve process for lube dewaxing by wax isomerization, Microporous Mater. 2 (1994) 439–449, https://doi.org/10.1016/0927-6513(94)00016-6.
[3] H. Heinemann, G.A. Mills, J.B. Hattman, F.W. Kirsch, Houdriforming reactions: studies with pure hydrocarbons, Ind. Eng. Chem. 45 (1953) 130–134, https://doi.org/10.1021/ie50517a042.
[4] H.L. Coonradt, W.E. Garwood, Mechanism of hydrocracking. reactions of paraffins and olefins, Ind. Eng. Chem. Process Des. Dev. 3 (1964) 38–45, https://doi.org/10.1021/i260009a010.
[5] P.B. Weisz, E.W. Swegler, Stepwise Reaction on Separate Catalytic Centers: Isomerization of Saturated Hydrocarbons, Science 126 (1957) 31–32, https://doi.org/10.1126/science.126.3262.31.
[6] P.B. Weisz, Polyfunctional heterogeneous catalysis, Adv. Catal. 13 (1962) 137–190, https://doi.org/10.1016/S0360-0564(08)60287-4.
[7] A.J. Jones, E. Iglesia, The strength of brønsted acid sites in microporous aluminosilicates, ACS Catal. 5 (2015) 5741–5755, https://doi.org/10.1021/acscatal.5b01133.
[8] R. Gounder, E. Iglesia, The catalytic diversity of zeolites: confinement and solvation effects within voids of molecular dimensions, Chem. Commun. 49 (2013) 3491–3509, https://doi.org/10.1039/c3cc40731d.
[9] A.J. Jones, S.I. Zones, E. Iglesia, Implications of transition state confinement within small voids for acid catalysis, J. Phys. Chem. C. 118 (2014) 17787–17800, https://doi.org/10.1021/jp5050095.
[10] S. Herrmann, E. Iglesia, Elementary steps in acetone condensation reactions catalyzed by aluminosilicates with diverse void structures, J. Catal. 346 (2017) 134–153, https://doi.org/10.1016/j.jcat.2016.12.011.
[11] M.L. Sarazen, E. Doskocil, E. Iglesia, Catalysis on solid acids: Mechanism and catalyst descriptors in oligomerization reactions of light alkenes, J. Catal. 344 (2016) 553–569, https://doi.org/10.1016/j.jcat.2016.10.010.
[12] C.L. Cavalcante, D.M. Ruthven, Adsorption of branched and cyclic paraffins in silicalite. 2. Kinetics, Ind. Eng. Chem. Res. 34 (1995) 185–191.
[13] B.D. Vandegehuchte, J.W. Thybaut, G.B. Marin, Unraveling diffusion and other shape selectivity effects in ZSM-5 using n-hexane hydroconversion single-event microkinetics, Ind. Eng. Chem. Res. 53 (2014) 15333–15347, https://doi.org/10.1021/ie500164q.
[14] W. Knaeble, R.T. Carr, E. Iglesia, Mechanistic interpretation of the effects of acid strength on alkane isomerization turnover rates and selectivity, J. Catal. 319 (2014) 283–296, https://doi.org/10.1016/j.jcat.2014.09.005.
[15] W. Knaeble, E. Iglesia, Acid strength and metal-acid proximity effects on methylcyclohexane ring contraction turnover rates and selectivities, J. Catal. 344 (2016) 817–830, https://doi.org/10.1016/j.jcat.2016.08.007.
[16] E. Verheyen, C. Jo, M. Kurttepeli, G. Vanbutsele, E. Gobechiya, T.I. Korányi, S. Bals, G. Van Tendeloo, R. Ryoo, C.E.A. Kirschhock, J.A. Martens, Molecular shape-selectivity of MFI zeolite nanosheets in n-decane isomerization and hydrocracking, J. Catal. 300 (2013) 70–80, https://doi.org/10.1016/j.jcat.2012.12.017.
[17] A. Soualah, J.L. Lemberton, L. Pinard, M. Chater, P. Magnoux, K. Moljord, Hydroconversion of n-decane on Pt/HZSM-5 bifunctional catalysts: Effect of the Si/Al ratio of the zeolite on selectivities, React. Kinet. Mech. Catal. 101 (2010) 209–219, https://doi.org/10.1007/s11144-010-0193-z.
[18] J. Weitkamp, P.A. Jacobs, J.A. Martens, Isomerization and hydrocracking of C9 through C16 n-alkanes on Pt/HZSM-5 zeolite, Appl. Catal. 8 (1983) 123–141, https://doi.org/10.1016/0166-9834(83)80058-X.
[19] K. Park, S. Ihm, Comparison of Pt/zeolite catalysts for n-hexadecane hydroisomerization, Appl. Catal. A Gen. 203 (2000) 201–209, https://doi.org/10.1016/S0926-860X(00)00490-7.
[20] Y. Bi, G. Xia, W. Huang, H. Nie, Hydroisomerization of long chain n-paraffins: the role of the acidity of the zeolite, RSC Adv. 5 (2015) 99201–99206, https://doi.org/10.1039/C5RA13784E.
[21] W. Zhang, P.G. Smirniotis, Effect of zeolite structure and acidity on the product selectivity and reaction mechanism forn-octane hydroisomerization and hydrocracking, J. Catal. 182 (1999) 400–416, https://doi.org/10.1006/jcat.1998.2337.
[22] A. Corma, A. Martinez, S. Pergher, S. Peratello, C. Perego, G. Bellusi, Hydrocracking-hydroisomerization of n-decane on amorphous silica-alumina with uniform pore diameter, Appl. Catal. A Gen. 152 (1997) 107–125, https://doi.org/10.1016/S0926-860X(96)00338-9.
[23] J. Kärger, D.M. Ruthven, D.N. Theodorou, Diffusion in Nanoporous Materials, Wiley-VCH, Weinheim, Germany (2012), https://doi.org/10.1002/9783527651276.ch18.
[24] G.W. Skeels, D.W. Breck, Silicon Substituted Y Zeolite Composition LZ-210, 4711770A, 1987.
[25] M. Choi, K. Na, J. Kim, Y. Sakamoto, O. Terasaki, R. Ryoo, Stable single-unit-cell nanosheets of zeolite MFI as active and long-lived catalysts, Nature. 461 (2009), https://doi.org/10.1038/nature08493, 828–828.
[26] C.D. Baertsch, K.T. Komala, Y.-H. Chua, E. Iglesia, Genesis of Brønsted acid sites during dehydration of 2-butanol on tungsten oxide catalysts, J. Catal. 205 (2002) 44–57, https://doi.org/10.1006/jcat.2001.3426.
[27] C. Baerlocher, L. McCusker, Database of Zeolite Structures, (n.d.). <http://www.iza-structure.org/databases/>.
[28] J.B. Higgins, R.B. LaPierre, J.L. Schlenker, A.C. Rohrman, J.D. Wood, G.T. Kerr, W.J. Rohrbaugh, The framework topology of zeolite beta, Zeolites 8 (1988) 446–452, https://doi.org/10.1016/S0144-2449(88)80219-7.
[29] M.M.J. Treacy, J.M. Newsam, Two new three-dimensional twelve-ring zeolite frameworks of which zeolite beta is a disordered intergrowth, Nature. 332 (1988) 249–251, https://doi.org/10.1038/332249a0.
[30] R.A. Alberty, C.A. Gehrig, Standard chemical thermodynamic properties of alkane isomer groups, J. Phys. Chem. Ref. Data. 13 (1984) 1173–1197, https://doi.org/10.1063/1.555726.
[31] R.A. Alberty, C.A. Gehrig, Standard chemical thermodynamic properties of alkene isomer groups, J. Phys. Chem. Ref. Data. 14 (1985) 803, https://doi.org/10.1063/1.555737.
[32] L. Karwacki, M.H.F. Kox, D.A. Matthijs de Winter, M.R. Drury, J.D. Meeldijk, E. Stavitski, W. Schmidt, M. Mertens, P. Cubillas, N. John, A. Chan, N. Kahn, S.R.

Bare, M. Anderson, J. Kornatowski, B.M. Weckhuysen, Morphology-dependent zeolite intergrowth structures leading to distinct internal and outer-surface molecular diffusion barriers, Nat. Mater. 8 (2009) 959–965, https://doi.org/10.1038/nmat2530.

[33] J. Crank, The Mathematics of Diffusion, second ed., Oxford University Press, 1980.

[34] J. Xiao, J. Wei, Diffusion mechanism of hydrocarbons in zeolites—I. Theory, Chem. Eng. Sci. 47 (1992) 1123–1141, https://doi.org/10.1016/0009-2509(92)80236-6.

[35] G. Kresse, J. Hafner, Ab initio molecular dynamics for liquid metals, Phys. Rev. B. 47 (1993) 558–561, https://doi.org/10.1103/PhysRevB.47.558.

[36] G. Kresse, J. Hafner, Ab initio molecular-dynamics simulation of the liquid-metal–amorphous-semiconductor transition in germanium, Phys. Rev. B. 49 (1994) 14251–14269, https://doi.org/10.1103/PhysRevB.49.14251.

[37] G. Kresse, J. Furthmüller, Efficient iterative schemes for ab initio total-energy calculations using a plane-wave basis set, Phys. Rev. B. 54 (1996) 11169–11186, https://doi.org/10.1103/PhysRevB.54.11169.

[38] G. Kresse, J. Furthmüller, Efficiency of ab-initio total energy calculations for metals and semiconductors using a plane-wave basis set, Comput. Mater. Sci. 6 (1996) 15–50, https://doi.org/10.1016/0927-0256(96)00008-0.

[39] J.P. Perdew, K. Burke, M. Ernzerhof, Generalized gradient approximation made simple, Phys. Rev. Lett. 77 (1996) 3865–3868, https://doi.org/10.1103/PhysRevLett. 77.3865.

[40] K. Yang, J. Zheng, Y. Zhao, D.G. Truhlar, Tests of the RPBE, revPBE, ?? -HCTHhyb, ??b97X-D, and MOHLYP density functional approximations and 29 others against representative databases for diverse bond energies and barrier heights in catalysis, J. Chem. Phys. 132 (2010), https://doi.org/10.1063/1.3382342.

[41] G. Kresse, From ultrasoft pseudopotentials to the projector augmented-wave method, Phys. Rev. B. 59 (1999) 1758–1775, https://doi.org/10.1103/PhysRevB.59.1758.

[42] P.E. Blöchl, Projector augmented-wave method, Phys. Rev. B. 50 (1994) 17953–17979, https://doi.org/10.1103/PhysRevB.50.17953.

[43] S. Grimme, J. Antony, S. Ehrlich, H. Krieg, A consistent and accurate ab initio parametrization of density functional dispersion correction (DFT-D) for the 94 elements H-Pu, J. Chem. Phys. 132 (2010), https://doi.org/10.1063/1.3382344.

[44] S. Grimme, S. Ehrlich, L. Goerigk, Effect of the damping function in dispersion corrected density functional theory, J. Comput. Chem. 32 (2011) 1456–1465, https://doi.org/10.1002/jcc.21759.

[45] H. Van Koningsveld, H. Van Bekkum, J.C. Jansen, On the location and disorder of the tetrapropylammonium (TPA) ion in zeolite ZSM-5 with improved framework accuracy, Acta Crystallogr. Sect. B. 43 (1987) 127–132, https://doi.org/10.1107/S0108768187098173.

[46] D.H. Olson, G.T. Kokotailo, S.L. Lawton, W.M. Meier, Crystal structure and structure-related properties of ZSM-5, J. Phys. Chem. 85 (1981) 2238–2243, https://doi.org/10.1021/j150615a020.

[47] A.J. Jones, R.T. Carr, S.I. Zones, E. Iglesia, Acid strength and solvation in catalysis by MFI zeolites and effects of the identity, concentration and location of framework heteroatoms, J. Catal. 312 (2014) 58–68, https://doi.org/10.1016/j.jcat.2014.01.007.

[48] H. Jónsson, G. Mills, K.W. Jacobsen, Nudged elastic band method for finding minimum energy paths of transitions, in: B.J. Berne, G. Ciccotti, D.F. Coker (Eds.), Class. Quantum Dyn. Condens. Phase Simulations Proc. Int. Sch. Phys., 1997.

[49] G. Henkelman, H. Jónsson, A dimer method for finding saddle points on high dimensional potential surfaces using only first derivatives, J. Chem. Phys. 111 (1999) 7010–7022, https://doi.org/10.1063/1.480097.

[50] P. Löwdin, On the nonorthogonality problem connected with the use of atomic wave functions in the theory of molecules and crystals, J. Chem. Phys. 18 (1950), https://doi.org/10.1063/1.1747632, 365–275.

[51] X. Qian, J. Li, L. Qi, C.Z. Wang, T.L. Chan, Y.X. Yao, K.M. Ho, S. Yip, Quasiatomic orbitals for ab initio tight-binding analysis, Phys. Rev. B Condens. Matter Mater. Phys. 78 (2008) 1–22, https://doi.org/10.1103/PhysRevB.78.245112.

[52] T.L. Chan, Y.X. Yao, C.Z. Wang, W.C. Lu, J. Li, X.F. Qian, S. Yip, K.M. Ho, Highly localized quasiatomic minimal basis orbitals for Mo from ab initio

calculations, Phys. Rev. B - Condens. Matter Mater. Phys. 76 (2007) 1–10, https://doi.org/10.1103/PhysRevB.76.205119.

[53] W.C. Lu, C.Z. Wang, M.W. Schmidt, L. Bytautas, K.M. Ho, K. Ruedenberg, Molecule intrinsic minimal basis sets. I. Exact resolution of ab initio optimized molecular orbitals in terms of deformed atomic minimal-basis orbitals, J. Chem. Phys. 120 (2004) 2629–2637, https://doi.org/10.1063/1.1638731.

[54] W.C. Lu, C.Z. Wang, T.L. Chan, K. Ruedenberg, K.M. Ho, Representation of electronic structures in crystals in terms of highly localized quasiatomic minimal basis orbitals, Phys. Rev. B Condens. Matter Mater. Phys. 70 (2004) 1–4, https://doi.org/10.1103/PhysRevB.70.041101.

[55] M.L. Connolly, Analytical molecular surface calculation, J. Appl. Crystallogr. 16 (1983) 548–558, https://doi.org/10.1107/S0021889883010985.

[56] C.T. Campbell, J.R.V. Sellers, Enthalpies and Entropies of Adsorption on Well-Defined Oxide Surfaces: Experimental Measurements, Chem. Rev. 113 (2013) 4106–4135, https://doi.org/10.1021/cr300329s.

[57] A. Bondi, van der Waals Volumes and Radii, J. Phys. Chem. 68 (1964) 441–451, https://doi.org/10.1021/j100785a001.

[58] H.S. Fogler, Elements of Chemical Reaction Engineering, fourth ed., Prentice Hall, 2005.

[59] M.F.M. Post, J. van Amstel, H.W. Kouwenhoven, Proceedings 6th International Conference on Zeolites Reno, Nevada, in: A. Bisio, D. Olson (Eds.), Proc. 6th Int. Conf. Zeolites Reno, Nevada, Butterworths, Guildford, UK, 1983. p. 517.

[60] M. Boronat, P. Viruela, A. Corma, A. Theoretical, Study on the mechanism of the superacid-catalyzed unimolecular isomerization of n -alkanes and n -alkenes. Comparison between ab initio and density functional results, J. Phys. Chem. 100 (1996) 16514–16521, https://doi.org/10.1021/jp961179w.

[61] M.A. Natal-Santiago, R. Alcalá, J.A. Dumesic, DFT study of the isomerization of hexyl species involved in the acid-catalyzed conversion of 2-methyl-pentene-2, J. Catal. 181 (1999) 124–144, https://doi.org/10.1006/jcat.1998.2293.

[62] V.B. Kazansky, Adsorbed carbocations as transition states in heterogeneous acid catalyzed transformations of hydrocarbons, Catal. Today. 51 (1999) 419–434, https://doi.org/10.1016/S0920-5861(99)00031-0.

[63] S. Wang, E. Iglesia, Catalytic diversity conferred by confinement of protons within porous aluminosilicates in Prins condensation reactions, J. Catal. 352 (2017) 415–435, https://doi.org/10.1016/j.jcat.2017.06.012.

[64] K. Chaudhari, T.K. Das, A.J. Chandwadkar, S. Sivasanker, Mesoporous Aluminosilicate of the MCM-41 Type: Its Catalytic Activity in n-Hexane Isomerization, J. Catal. 186 (1999) 81–90, https://doi.org/10.1006/jcat.1999.2533.

[65] A. Corma, A. Martinez, V. Martinezsoria, J.B. Monton, Hydrocracking of Vacuum Gasoil on the Novel Mesoporous MCM-41 Aluminosilicate Catalyst, J. Catal. 153 (1995) 25–31, https://doi.org/10.1006/jcat.1995.1104.

[66] G. Noh, Catalytic Consequences of Metal-Acid Site Proximity, Acid Strength, and Confinement on Bifunctional Transformations of Alkanes, University of California, Berkeley, 2017.

[67] J.S. Buchanan, J.G. Santiesteban, W.O. Haag, Mechanistic considerations in acid-catalyzed cracking of olefins, J. Catal. 158 (1996) 279–287, https://doi.org/10.1006/jcat.1996.0027.

[68] R. Gounder, A.J. Jones, R.T. Carr, E. Iglesia, Solvation and acid strength effects on catalysis by faujasite zeolites, J. Catal. 286 (2012) 214–223, https://doi.org/10.1016/j.jcat.2011.11.002.

[69] M. Aronson, R.J. Gorte, W.E. Farneth, The influence of oxonium ion and carbenium ion stabilities on the alcohol/H-ZSM-5 interaction, J. Catal. 98 (1986) 434–443, https://doi.org/10.1016/0021-9517(86)90331-3.

[70] P. Deshlahra, E. Iglesia, Toward more complete descriptors of reactivity in catalysis by solid acids, ACS Catal. 6 (2016) 5386–5392, https://doi.org/10.1021/acscatal.6b01402.

[71] E.W. Thiele, Relation between Catalytic Activity and Size of Particle, Ind. Eng. Chem. 31 (1939) 916–920, https://doi.org/10.1021/ie50355a027.

[72] K.B. Bischoff, Effectiveness factors for general reaction rate forms, AIChE J. 11 (1965) 351–355, https://doi.org/10.1002/aic.690110229.

[73] J. Xiao, J. Wei, Diffusion mechanism of hydrocarbons in zeolites-II. Analysis of experimental observations, Chem. Eng. Sci. 47 (1992) 1143–1159, https://doi.org/10.1016/0009-2509(92)80237-7.